IEEE Access
Multidisciplinary | Rapid Review | Open Access Journal

Received February 23, 2019, accepted March 10, 2019, date of publication March 13, 2019, date of current version April 5, 2019.

Digital Object Identifier 10.1109/ACCESS.2019.2904709

A Novel Weight-Bearing Lower Limb Exoskeleton Based on Motion Intention Prediction and Locomotion State Identification

YUXIANG HUA[1], JIZHUANG FAN[1], GANGFENG LIU[1], (Member, IEEE), XUEHE ZHANG[1], MINGZHU LAI[2], MO LI[1], TIANJIAO ZHENG[1], GUOAN ZHANG[3], JIE ZHAO[1], (Member, IEEE), AND YANHE ZHU[1], (Member, IEEE)

[1]State Key Laboratory of Robotics and System, Harbin Institute of Technology, Harbin 150001, China
[2]School of Mathematics and Statistics, Hainan Normal University, Haikou 571158, China
[3]School of Aeronautical Engineering, Taizhou University, Taizhou 318000, China

Corresponding authors: Jizhuang Fan (fanjizhuang@hit.edu.cn), Gangfeng Liu (liugangfeng@hit.edu.cn), Xuehe Zhang (zhangxuehe@hit.edu.cn), Mingzhu Lai (laimingzhu@126.com), and Yanhe Zhu (yhzhu@hit.edu.cn)

This work was supported in part by the National Key R&D Program of China under Grant 2018YFB1305400, in part by the Joint Research Fund between the National Nature Science Foundation of China (NSFC) and Shenzhen under Grant U1713201, and in part by the National Key R&D Program of China under Grant 2017YFB1302301.

ABSTRACT A variable magnification ratio transmission structure powered by the electric actuators is proposed to improve the flexibility and portability of the exoskeleton under heavy load carrying condition. The parameters of connecting rod size and hanging position are optimized to ensure that the output torque of active joints can fully envelope the demand load area. The control strategy based on intrinsic sensing is designed to realize the automatic human motion intention prediction and flexible trajectory tracking. The newly developed split embedded connecting rod can accurately measure the human–robot interaction (HRI) force applied to the exoskeleton and extract the human motion intention without being affected by the differences in wearing status. The force tracking control based on the zero-force following is modified by feedforward compensation with extreme learning machine (ELM), which enhances the response speed to human motion intention and reduces the HRI force by 70.6%. Based on multi-sensor information, stacked autoencoder deep neural networks (DNNs) are utilized to realize the automatic locomotion transition and the corresponding control parameters' switching. After optimization by a hybrid algorithm of genetic algorithm and particle swarm optimization (GA_PSO), the identification accuracy is enhanced from 96.2% to 99.7%. The adaptive neural-fuzzy inference system (ANFIS) is used to analyze the plantar pressure to achieve flexible switching between the swing phase and the stance phase. The experiments under various gait motion trajectories assisted by novel weight-bearing exoskeleton are carried out for evaluation, and the performance of the proposed control strategy based on motion intention prediction, locomotion mode identification, and gait phase switching is effectively verified.

INDEX TERMS Variable magnification ratio structure, intrinsic sensing, intention prediction, locomotion state identification, GA_PSO, DNNs, ANFIS, robotic exoskeletons.

I. INTRODUCTION

Weight-bearing lower limb exoskeletons are widely used to assist the human body to enhance muscular strength for bearing extra loads, improving body function and reducing metabolic cost. Recent notable research on enhancing load-carrying capabilities and related technology have extended applications to practical areas [1]–[3]. Aiming to enable super-soldiers for carrying large quantities of military capital, high-speed marching, and mixed operations on complex roads, research groups at the University of California successively developed the Berkeley lower extremity exoskeleton (BLEEX) [4], ExoHiker & ExoClimber and the human universal load carrier (HULC) [5]. Under the support of the Exoskeleton for Human Performance Augmentation (EHPA) project, the company Sarcos has also developed a series of hydraulically driven full-body exoskeletons that can perform complex movements such as running, jumping, kicking and push-ups [6]. The power assisting suit (PAS) developed by the Kanagawa Institute of Technology is powered by pneumatic actuators arranged in the joints of the shoulder,

The associate editor coordinating the review of this manuscript and approving it for publication was Tao Liu.

elbow, hip and knee to assist nurses in the daily care and rehabilitation of patients [7]. Arranging the actuators in the same way as the PAS, the active joints of the wearable agri-robot (WAR) developed by the University of Tokyo are driven by ultrasonic motors to alleviate the physical burden in the labor process [8]. The hybrid assistive limb (HAL) developed by the University of Tsukuba [9] and the HERCULE V3 developed by RB3D [10] have two sets of electricity-powered servo actuators placed on the knee and hip joints; these actuators help reduce the burden on the waist when the upper limbs are used to lift heavy objects. Despite these efforts, a number of technological challenges remain in research on assistance efficiency, energy consumption, lightweight structure and actuator system maintainability. Although hydraulic and pneumatic systems can provide larger output torque than electricity-powered actuators, the system circuits are complicated, the maintenance cost is high, the overall weight is large, and the energy utilization efficiency is low. In addition, improvements in portability and weight reduction are needed. The linear telescopic cylinder as the output device needs to be arranged outside the rotating joint, and the hinge hanging points at both ends are respectively arranged on the thigh and the calf structure. The underlying principle is to change the length of one side of the triangle to achieve changes in the joint angle and driving torque [11]. When the output torque reaches the peak point according to this arrangement, the required telescopic rod and the occupied space are larger [12], [13]. The use of servo motors as the power source increases the accuracy of the torque control effect, and the system is easier to maintain and adjust. However, if the active joint is directly driven by the gear pairs facilitates, although the transmission form and implementation is easy, the torque transmission for heavy loads requires large-diameter gears and high-power motors which should be avoided in compact structure design. In addition, the applied load torque increases with the joint angle when the joint bends in the stance phase [14]–[16]. Since the bevel gear transmission structure can only output a constant torque, resulting in poor torque availability and guarantee of torque demand at various positions during the motion trajectory. Therefore, it is necessary to design a variable magnification ratio structure actuated by servo motors so that the output torque under heavy-load-carrying conditions can completely envelope the load demand area, improve the utilization of the motor rated torque, minimize the weight of the structure and increase the mobility and portability of the exoskeleton to the utmost extent.

As the exoskeleton is a wearable operating system dominated by human consciousness, the control strategy needs to incorporate the human body into the control system and consider interventions caused by behavioral differences. For precise tracking control, the exoskeleton needs to have the ability to perceive the human motion intention based on large quantities of interaction information in the human-machine coupling system. The electromyography (EMG) feedback signals and joint angles are analyzed to establish the mapping relationship between motor torques and EMG signals [17], [18]. Through the brain-computer interface, VR technology and mechatronics control technology, the virtual environment exoskeleton rehabilitation platform of the Mindwalker is built so that patients can use electroencephalograph (EEG) signals to achieve real-time operation of the exoskeleton [19]. The lower extremity powered exoskeleton (LOPES) [20] and the HIT-LEX [21] measure the human-robot interaction (HRI) force transferred on the bundle connectors to predict human motion intention.

The advantage of the above methods is that they can directly extract the interaction. However, the main drawback is mainly manifested in the aspect that since the bundling components are generally placed at the connection position with the thigh, the calf and the foot, the measured HRI forces vary with the wearing status and physical response of the human body, which will lead to measurement deviations and decoupling interference of the HRI value. Thus, an adaptive control strategy based on intrinsic sensing is necessary to ensure that the extraction of HRI is independent of wearing status [22]. Since the connecting rod is both a transmission component and an elastic measuring and sensing unit in the transmission structure, the arrangement positions of the connecting rod determine the size and force characteristics. After assembly and installation, measurement is directly performed by the intrinsic sensing, which avoids structural redundancy, initial deviation and additional calibration due to the bundling of new wearers. As the transferred HRI extracted from to the mechanism usually lags behind the actual intention, feedforward compensation can enhance the response speed of the control system for precision tracking control [23], [24]. As a machine learning algorithm with high learning efficiency and generalization ability, the extreme learning machine (ELM) is utilized in prediction estimation [25]. Combined with the tracking differentiator (TD), ELM can predict the multi-order differential signals with a smaller phase delay compared with the associated method of Kalman-filter-based forecast and differential derivation.

In real working situations, it is necessary to know the locomotion mode condition and switch the corresponding control parameters to complete tasks. In addition, an adaptive smooth locomotion transition can enhance safety and balance to achieve a more natural gait trajectory. Based on the extracted signals from the exoskeleton system, an efficient and precise locomotion state identification method for the locomotion mode and gait phase is required. In machine learning, it is difficult to search for a good classification model even if the what-if space contains good hypotheses, especially when the data quantity is too large and the feature extraction is poor. Furthermore, Yuan et al. noted that a good terrain identification method should meet four requirements, including high identification accuracy, minimal sensors embedded into the mechanism, short identification delay, and low computation load [26]. Although the introduction of kernel principal component analysis (kPCA) and other methods can reduce

the data dimension and the computational cost of the algorithm to a certain extent [27], the extraction of the original data features will be affected, and the improvement of the identification speed is not obvious. Seeking intelligent feature extraction methods and improving identification efficiency are still the focus of machine learning. In deep learning, since convolutional neural networks (CNNs) uses convolution kernels for feature extraction and feature mapping in selected regions, images of complex features and high-dimensional matrices can be effectively identified [28], [29]. However, as the poorly correlated exoskeleton sensor information mixed with joint angles, the measured HRI force and other intrinsic feature signals are arranged into a two-dimensional matrix as data samples for training, it is difficult to accurately identify various locomotion modes due to the lower dimensionality. For deep neural networks (DNNs), the weights obtained from unsupervised learning can be used as the initial values of the subsequent supervised learning for deeper training. In the structure of the stacked autoencoder DNNs, the lower layer neurons are fully connected with all upper layer neurons, which successfully improves the identification accuracy significantly [30], [31]. Therefore, DNNs is more suitable for intelligent feature extraction and high-precision locomotion mode identification of medium-dimensional data compared with machine learning and CNNs.

However, the identification accuracy is mainly affected by the key parameters in the network structure, such as the weight regularization, sparsity regularization and sparsity proportion. To obtain the optimal parameter settings in the training, several optimization methods such as grid search [32], genetic algorithm [33], and PSO [34] have been used with success. If the initial positions in the GA optimization process are inappropriate, the optimization result may fall into a local optimum, which often leads to premature convergence of the solution and convergence error. Although the PSO algorithm has high precision, the global convergence speed is usually slow. To ensure the rapid convergence of the control system and maintain stability, the GA algorithm is used to modify the PSO algorithm, and the GA_PSO is finally selected to optimize the neural network parameters [35], [36].

Since the kinetic equations of the exoskeleton in the stance phase and the swing phase are based on different pedestal points, it is necessary to switch the corresponding control models and parameters to calculate the joint output torque during the motion trajectory. The ground reaction force (GRF) is collected using a wearable plantar pressure measurement system to judge the phase state of a single leg based on its numerical change when the exoskeleton contacts the ground [37]. However, separating the swing phase and the support phase according to the critical region alone may cause oscillation at the time of switching, and the determination of the critical value has higher requirements for the repeatability of gait and the stability of pressure values. Therefore, a classifier with strong generalization ability is necessary for accurate phase switching. A hybrid identification method adaptive neural-fuzzy inference system (ANFIS) that combines the adaptive learning ability of a neural network and the inference analysis of a fuzzy system is used as an automated learning tool for identification [38], [39]. Instead of depending on the adequacy of training samples, the identification performance remains accurate owing to the strong generalization ability.

Therefore, a novel lower limb exoskeleton actuated by a variable magnification ratio structure is developed in this paper. With optimization of the hanging points and structure parameters, the output torque can fully envelop the demand load area and achieve compactness and a lightweight design for weight-lifting assistance. An intrinsic sensing prediction control strategy with ELM feedforward compensation is proposed to perceive the intention trajectory through the HRI force extracted from the split embedded connecting rod sensors assembled into the interior transmission structure. For automatic locomotion identification with multi-sensors, a hybrid GA_PSO optimized DNNs and ANFIS are separately utilized to identify the locomotion modes and gait phase. The corresponding verification experiments prove the notable performance of the proposed control strategy.

II. VARIABLE MAGNIFICATION RATIO STRUCTURE DESIGN AND PARAMETER OPTIMIZATION

As shown in Fig. 1, the lower limb exoskeleton is initially designed based on biological principles which is required to retain adaptability to the versatility and flexibility of the lower limbs. Aided by analysis of the enormous Clinical Gait Analysis (CGA) dataset of human locomotion features, the active hip joint and knee joint are actuated by screw-crank-slider units driven by EC servo motors.

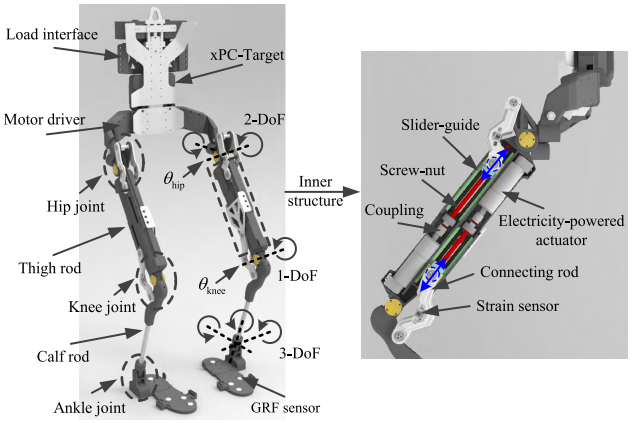

FIGURE 1. The principle prototype of the electricity-powered lower limb exoskeleton.

The active DOFs of the hip and knee joints are arranged on the sagittal plane, which in turn supports the load in the direction of gravity. The passive DOFs of the hip joints are arranged on the frontal plane, allowing free follow-up for side-swing motion. In contrast to the transmission structure of the linear telescopic cylinder, the screw-crank-slider units ensure that the inertia center remains on the stroke plane of the screw when the active DOF joints move, accompanied by minor adjustments in a smaller range. The proposed arrange-

ment reduces the calculation of the dynamic center position of the connecting rod inertia and the approximation error caused by the simplified estimation when the dynamic model is established. Furthermore, the hip joint and knee joint can flexibly move within the range of −30° to 100° and 0° to 120° at large output torque when wearer works under the assistance of exoskeleton as shown in TABLE 1.

TABLE 1. Joint range of motion.

Joint	DOF	Range
Hip	Flexion/Extension	-30°--100°
	Adduction/Abduction	-30°--50°
Knee	Flexion/Extension	0°--120°
Ankle	Plantarflexion/Dorsiflexion	-35°--30°
	Pronation/External rotation	-25°--25°
	Inversion/Eversion	-25°--25°

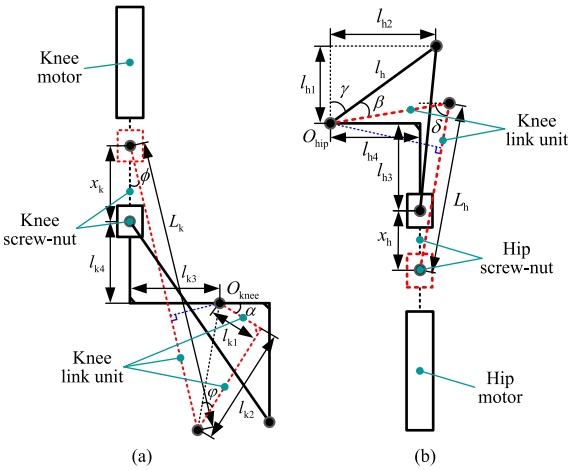

FIGURE 2. The schematic diagram of the variable magnification ratio transmission structure of the hip joint and knee joint.

As shown in Fig. 2, the motors of hip joint and knee joint are arranged in the opposite directions. In Fig. 2, l_{k1}, l_{k2}, l_{k3}, l_{k4}, L_k and l_{h1}, l_{h2}, l_{h3}, l_{h4}, L_h are distance parameters between hanging points and the rotating joints on the connecting rods. x_k, x_h are the available travel range of sliders. α, β are the joint angles of active knee and hip joints, and ϕ, φ, γ, δ are parametric angle variables. The size parameters of the connecting rod directly determine the magnification ratio of the transmission structure and the joint rotation ranges. Therefore, the actual demanded driving torque at all target positions during motion gaits should be satisfied on the basis of ensuring a lightweight, simplified transmission structure. According to the working principle of the crank-slider structure, the parameters of connecting rod size and the position of the hanging points are optimized.

Due to phase transition and shock buffering during motion gaits, it is difficult to obtain accurate torque characteristics directly from rigid body dynamics simulations. After establishing the human-exoskeleton-environment simulation platform, the co-simulation by Adams/Life-mod can acquire relatively referable joint torque characteristics when the exoskeleton bears an approximate maximum load of 55 kg. Therefore, the characteristics between joint angles and torques under the motion gaits of walking, squatting, stair ascent, and stair descent are obtained [14]–[16]. Based on the above simulated curves, the optimal parameters for the design of the crank-slider transmission structure are optimized to ensure that the motors working under rated conditions can meet the driving requirements during the corresponding gait motions.

According to the power conservation principle, the variable magnification ratio k_{knee} and k_{hip} of the transmission structure can be expressed as

$$\begin{cases} k_{knee} = l_{k2}\sin\alpha - l_{k1}\cos\alpha \\ \qquad + \dfrac{(l_{k3} + l_{k1}\cos\alpha - l_{k2}\sin\alpha)(l_{k1}\sin\alpha + l_{k2}\cos\alpha)}{\sqrt{L_k^2 - [l_{k3} + l_{k1}\cos\alpha - l_{k2}\sin\alpha]^2}} \\ k_{hip} = l_h\sin(\gamma+\beta) \\ \qquad - \dfrac{l_h\cos(\gamma+\beta)[l_h\sin(\gamma+\beta) - l_{h3}]}{\sqrt{L_h^2 - [l_h\sin(\gamma+\beta) - l_{h3}]^2}} \end{cases} \tag{1}$$

In the optimization process, the constraints are the screw stroke and the peak position of the magnification ratio. Thus, the constraint equations can be written as

$$\begin{cases} \dfrac{\partial T_{Jknee}}{\partial\alpha} = \dfrac{2\pi T_{Mknee}}{s} \cdot \dfrac{\partial k_{knee}(L_k, l_{k1}, l_{k2}, \alpha)}{\partial\alpha}\Big|_{\alpha=115.4^o} \doteq 0 \\ \dfrac{\partial T_{Jhip}}{\partial\beta} = \dfrac{2\pi T_{Mhip}}{s} \cdot \dfrac{\partial k_{hip}(L_h, l_h, \beta)}{\partial\beta}\Big|_{\beta=87.7^o} \doteq 0 \end{cases} \tag{2}$$

where T_{Jknee}, T_{Jhip} are driving torques transmitted to the active rotational joints of the exoskeleton, T_{Mknee}, T_{Mhip} are output torques provided by the electricity-powered motors, and s is the screw lead.

Optimizing the structure parameters of the connecting rod by taking the coverage area of the enveloping curve, the curve inflection point position and the screw stroke as constraints, the minimum reduction ratio for the actuator is reduced from 6 to 3.5, which makes the screw stroke retain enough margin after reducer is added and increases the maximum rotational speed of the joint and thus greatly improves the maneuverability under weight-bearing working conditions. The gray curves in Fig. 3 represent the rated output torque of the active joints through the magnification of the screw-crank-slider when the motors work under the rated conditions. The black curves represent the maximum envelope of the output torque by the transmission structure with optimized parameters. The colored dotted curves in the middle region represent the output characteristics during the four gait trajectories. Therefore, although the position of the torque extreme point deviates from demanded position, the output capacity at a small angle

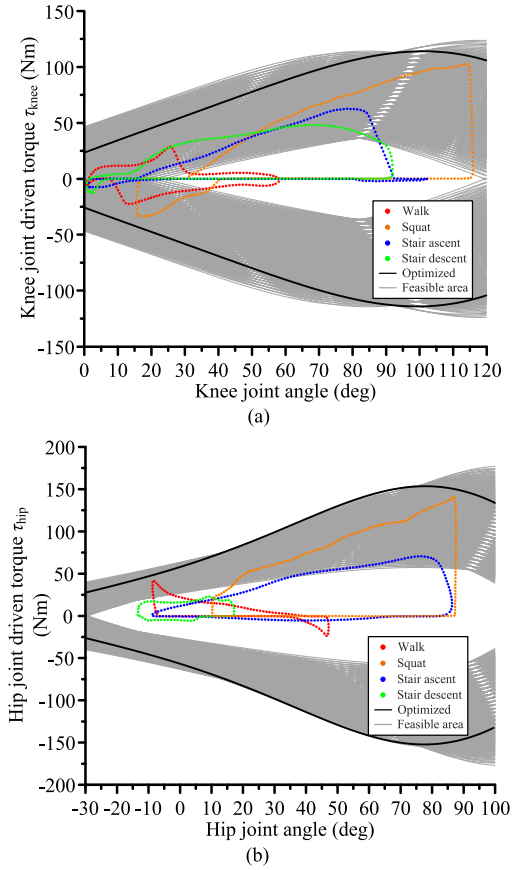

FIGURE 3. The output characteristic curves of joint torque during gait motions under heavy-load-carrying conditions.

range is greatly improved; thus, the output characteristics can satisfy the actual needs within the angular activity range and retain a certain margin. Thus, the optimization results have been effectively verified.

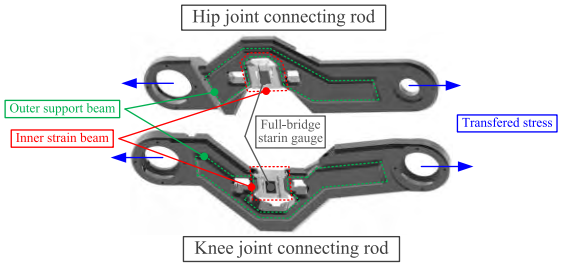

FIGURE 4. The structure of the connecting rod for measuring HRI force.

To obtain the transfer stress on the connecting rod and analyze the actual strain during gait cycles, finite element analysis based on ANSYS is carried out to arrange the position of force sensors to determine the range and minimum resolution. As shown in Fig. 4, the newly developed split embedded connecting rod is composed of three parts to measure the corresponding change: the outer support arm, which mainly bears the transmission torque and drives the screw-slider to rotate the hip joint and the knee joint freely; the inner strain beam, which amplifies the strain transferred on the outer support arm; and the full-bridge strain gauge group, which converts the strain into the physical quantity of the resistance value.

Based on the optimization result of the connecting rod structure, the characteristic length parameters and the hanging points can be obtained. According to the simulation curves of joint torques under different gait trajectories by the Adams/Life-mod co-simulation platform, the relationship between the applied driving force transferred on the connecting rod and the joint angle is extracted and then used to determine the range and resolution of the full-bridge strain sensor embedded in the connecting rod. Since the two ends of the connecting rod are bearing hinges and the stress direction passes through the line connecting the center points of the hinges at both ends, the connecting rod can be approximately regarded as a two-force rod. The connecting rod needs to be calibrated and tested to obtain the stiffness coefficient and resolution for extracting the HRI force.

According to the torque conservation principle, the torque calculation is performed on the rotation center of the active joints O_{knee} and O_{hip} respectively. The applied force transferred from the motor to the connecting rod is solved, and the mathematical expressions can be written as

$$\begin{cases} F_{\text{hip}} = \dfrac{T_{\text{Jhip}}}{l_{\text{h}} \sin[\arcsin[\frac{l_{\text{h}} \sin(\gamma+\beta)-l_{\text{h4}}}{L_{\text{h}}}] + \gamma + \beta - 90^{\text{o}}]} \\ F_{\text{knee}} = \dfrac{T_{\text{Jknee}}}{l_{\text{k}} \sin(\alpha - \varphi + \arcsin[\frac{l_{\text{k3}}+l_{\text{k1}} \cos\alpha - l_{\text{k2}} \sin\alpha}{L_{\text{k}}}])} \end{cases} \tag{3}$$

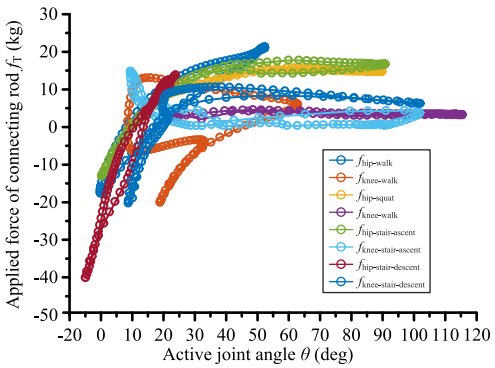

FIGURE 5. The applied force transmitted on the connecting rods during gait motions under load-carrying conditions.

Fig. 5 shows the relationship between the applied force and the joint angle during the four motion trajectories of walking, squatting, stair ascent and stair descent. When the exoskeleton is in the stance phase, the maximum force mainly appears in the process of load-carrying and the collision impact with the ground. The instantaneous acceleration produced by rapid motion will also increase the HRI value. Therefore, it needs to reserve sufficient margin over the measurement range. For the active knee joint when the human motion is in the swing phase, the angular velocity is larger and the motion range

is wider than that of the active hip joint, so the flexibility of the active knee joint is required to be higher. Thus, it is necessary to appropriately improve the detection resolution of HRI force of the knee joint, thereby improving the sensitivity of the joint motion, and quickly responding and tracking the human intended trajectory. According to the above requirements, the connecting rod is assembled and calibrated with the actual parameters shown in TABLE 2.

TABLE 2. Properties of optimized connecting RODS.

Parameters	Hip joint	Knee joint
Stiffness	18±1.2 /kgf	32±2.3 /kgf
Resolution	0.05 kg	0.1 kg
Measurement range	-75 kg--50 kg	-75 kg--50 kg
Horizontal offset L_1	84.5723 mm	10 mm
Longitudinal offset L_2	30.7818 mm	65 mm
Midline offset L_3	63.6147 mm	23 mm
Travel offset L_4	25 mm	86.4472 mm
Hinge span L_e	148 mm	155 mm

The original signal change of the force sensor on the connecting rod is amplified through AD8420 chip on the peripheral circuit and is transferred into the ADC pin of STM32F103C8T6. The stiffness in the table II represents that if 1kgf force is applied at both ends of the connecting rod, the signal change measured in the digital circuit is 18±1.2 for hip joint and 32±2.3 for knee joint. Full scale of ADC signal in the chip is 4096 respected to 3.3V in the form of analog signal. The HRI force in this paper is expressed in the form of digital signal, which is more convenient compared with the expression in the form of analog signal, and is easy for numerical conversion in the following HRI curves.

III. INTRINSIC SENSING PREDICTION CONTROL STRATEGY WITH FEEDFORWARD COMPENSATION

A. INTRINSIC SENSING FOR MOTION INTENTION

By introducing the previous system structure, the crank-connecting rod-screw structure is adopted to realize the power transmission of the electric actuators. Therefore, the strain gauge sensor based on the full-bridge circuit embedded on the connecting rod can directly detect the HRI force driven to the exoskeleton structure. According to the force analysis on the transfer process, the resultant driving force on the connecting rod is decomposed into two parts:

$$F_{\mathrm{L}} = \xi(\theta) F_{\mathrm{gravity}} + f_{\mathrm{HRI}} \tag{4}$$

To compensate for the error of the gravity term caused by model estimation and the dynamic gap, it is necessary to calibrate the load force generated by the gravity term F_{gravity} at each joint angular position during static equilibrium. In the subsequent extraction of human-robot interaction, the extracted HRI force can be corrected by a function expression $\xi(\theta)$, which is the ratio between the actually measured value and the theoretical analysis value. To describe the functional relationship between the human body and exoskeleton, the mathematical expression of HRI is equivalent to a simplified spring model:

$$f_{\mathrm{HRI}} = K(\hat{\theta}_{\mathrm{d}} - \theta) \tag{5}$$

where K is the stiffness coefficient of the connecting rod.

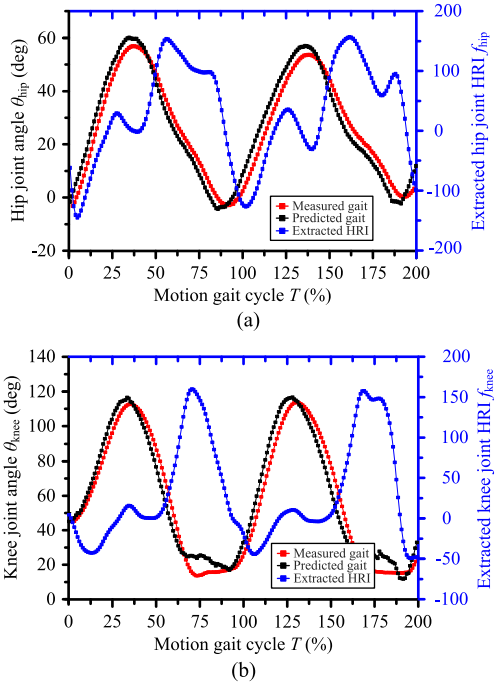

FIGURE 6. The intrinsic sensing prediction of human intended motion trajectory.

The noise filter is designed to smooth the HRI force signal online, and the demanded autonomous motion trajectory of the human body can be extracted as shown in Fig. 6. The HRI force has a fixed phase deviation with the desired trajectory under actual conditions that remains stable within a certain amplitude and frequency bandwidth. The HRI is generated ahead of the actual movement of the exoskeleton, which allows the system to update the desired gait trajectory. Since the desired motion trajectory is determined by the human body's intention and the HRI model cannot be universally defined, the parameters need to be adjusted through personalized customization according to comfort and followability in actual experiments. If a parameter is too small, it will lead to serious hysteresis of following, making human body exercise difficult. If a parameter is too large, the system movement will be ahead of the human intention, which will interfere with human motions and bring obstacles.

B. CONTROL STRATEGY WITH FEEDFORWARD COMPENSATION

To accurately extract the predictive multi-order differential signals at the next control cycle, a combination of ELM and

TD is introduced in the control strategy. The step-varying TD is superior to the traditional differential calculation method for extracting multi-order differential signals for discontinuous signals with random noise. Based on the filtered signals and their differentiated signals, the initial signals and the phase delays produced through TD are compensated by prediction. Good results can be obtained by the adoption of step-varying TD and prediction under the condition of the sampled signal with noise and varying sampling time. The tracking form $\theta_{\mathrm{T}}^{k+1}$ and derivative form $\theta_{\mathrm{TD}}^{k+1}$ of the original signal are

$$\begin{cases} \theta_{\mathrm{T}}^{k+1} = \theta_{\mathrm{T}}^{k} + h \cdot \theta_{\mathrm{TD}}^{k} \\ \theta_{\mathrm{TD}}^{k+1} = \theta_{\mathrm{TD}}^{k} - \delta \cdot sat(g^k, \delta) \end{cases} \tag{6}$$

where $\delta = rh$, h is the length of the integral step, r defines the speed of tracking, and $sat(g^k, \delta)$ is the piecewise function. If the condition $g^k \geq \delta$ is true, the piecewise function is equivalent to $sign(g^k)$. Otherwise, it equals g^k/δ.

The mathematical expression of g^k is given as [40]

$$g^k = \begin{cases} \theta_{\mathrm{TD}}^{k} + sign(y^k) \cdot \dfrac{\sqrt{8r\left|y^k\right| + \delta^2} - \delta}{2}, & \left|y^k\right| \geq \delta h \\ \theta_{\mathrm{TD}}^{k} + \dfrac{y^k}{h}, & \left|y^k\right| < \delta h \end{cases} \tag{7}$$

where $y^k = \theta_{\mathrm{TD}}^{k} - \theta^k + h \cdot \theta_{\mathrm{TD}}^{k}$ represents the tracking error of TD. A larger r implies faster tracking of θ by θ_{T}^{k}. However, if the noise signal is doped into θ, it will affect the tracking of θ_{T}^{k}. To filter the noise of θ_{T}^{k}, choosing a proper h is necessary as it can filter more noise and compensate the phase loss between θ_{T}^{k} and θ.

ELM is a type of machine learning algorithm designed for Single Layer Feedforward neuron Network (SLFN). The main feature is that the hidden layer node parameters can be random or artificially given and do not need to be adjusted, and the learning process only needs to calculate the output weight. ELM has advantages of simple structure, high learning efficiency, strong generalization ability, and fast calculation speed and is quite suitable for online real-time prediction of high sampling frequency data. Supposing that there are N arbitrary samples (x_j, t_j), where the input and the output are respectively $x_j = [x_{j1}, x_{j2}, \ldots, x_{jn}]^{\mathrm{T}} \in R^n$ and $t_j = [t_{j1}, t_{j2}, \ldots, t_{jm}]^{\mathrm{T}} \in R^m$. The learning goal for a single hidden layer neural network with L nodes is to minimize the output error $\left\|\mathrm{H}(\hat{w}_i, \hat{b}_i) \cdot \hat{\beta} - \mathrm{T}\right\| = \min_{w,b,\beta} \|\mathrm{H}(w_i, b_i) \cdot \beta - \mathrm{T}\|$, which is equivalent to minimizing the loss function [41]

$$E_{\mathrm{loss}} = \sum_{j=1}^{N} \left\| \sum_{i=1}^{L} \beta_i g(w_i \cdot x_j + b_i) - t_j \right\|_2^2 \tag{8}$$

where w_i, b_i, g and β_i are the weight, offset, activation function and output weight of the neuron. Some traditional algorithms based on gradient descent can be used to solve such problems, but the basic gradient-based learning algorithm needs to adjust all parameters in an iterative process. Once the input weight and hidden layer offset are randomly set, the output matrix of the hidden layer is uniquely determined. Training a single hidden layer neural network can be transformed into solving a linear system, and the output weights can be calculated as $\hat{\beta} = \mathrm{H}^{+} \cdot \mathrm{T}$, where H^{+} is the Moore-Penrose generalized inverse matrix of H.

According to the negative feedback, feedforward HRI response and the PD controller, the demanded acceleration of the joint is

$$\tau_{\mathrm{d}} = K_{\mathrm{p}} K(\hat{\theta}_{\mathrm{d}} - \tilde{\theta}) + K_{\mathrm{d}} K(\dot{\hat{\theta}}_{\mathrm{d}} - \dot{\tilde{\theta}}) + \ddot{\hat{\theta}}_{\mathrm{d}} \tag{9}$$

where $\hat{\theta}_{\mathrm{d}}$ is the estimation of the demanded motion trajectory of the human body extracted by HRI force decomposition; K_{p} and K_{d} are parameters of the PD controller; and K is the stiffness of HRI spring model.

The basic condition for ultimate stability is that at the next control cycle the exoskeleton can accurately follow the actual autonomous intentional trajectory of the human body. Since hysteresis always exists during the HRI measurement and the system response, the ultimate prerequisite for achieving stability is to minimize HRI to the utmost extent. Since the exoskeleton is a typical robotic system with high coupling and inherent nonlinearity, we apply adaptive computed torque control to address this issue. Therefore, considering the real dynamic model without loss of generality, the control law for exoskeleton is given as the following:

$$\begin{aligned} T_{\mathrm{e}} = {} & M(\tilde{\theta})[K_{\mathrm{p}} K(\hat{\theta}_{\mathrm{d}} - \tilde{\theta}) + K_{\mathrm{d}} K(\dot{\hat{\theta}}_{\mathrm{d}} - \dot{\tilde{\theta}}) + \ddot{\hat{\theta}}_{\mathrm{d}}] \\ & + C(\dot{\tilde{\theta}}, \tilde{\theta})\dot{\hat{\theta}}_{\mathrm{d}} + G(\tilde{\theta}) + F(\dot{\tilde{\theta}}) - J^{\mathrm{T}} f \end{aligned} \tag{10}$$

where $M(\tilde{\theta})$, $C(\dot{\tilde{\theta}}, \tilde{\theta})$, $G(\tilde{\theta})$, $F(\dot{\tilde{\theta}})$ denote the estimations of the inertial matrix, the centrifugal and Coriolis term, the gravitational matrix, and friction interference, respectively, at each desired position during the next discrete control moment.

In the control loop without ELM prediction, the k-th measured gesture information is used to solve the control torque for the exoskeleton system. The currently measured gesture signals lead the phase ahead of the expected gesture signals at the next moment, causing the following motion to overtake the steady-state position and oscillate within its stable neighborhood. Consequently, the parameter tuning for discrete input signals becomes longer, and the response time of the exoskeleton system increases. With the addition of ELM prediction, it is possible to observe the expected position of the exoskeleton at the next moment, accurately compensate the inertia of the system, and improve the dynamic response of the system to make the driving torque calculated by the control law tend the practically demanded value.

The dynamic equation of the system at next control moment can be expressed as

$$M(\tilde{\theta})\ddot{\tilde{\theta}} + C(\dot{\tilde{\theta}}, \tilde{\theta})\dot{\tilde{\theta}} + G(\tilde{\theta}) + F(\dot{\tilde{\theta}}) = \tau + J^{\mathrm{T}} f \tag{11}$$

To verify the stability of the control system, the Lyapunov function is chosen as

$$V = \frac{1}{2} \dot{s}^{\mathrm{T}} M(\tilde{\theta}) \dot{s} \tag{12}$$

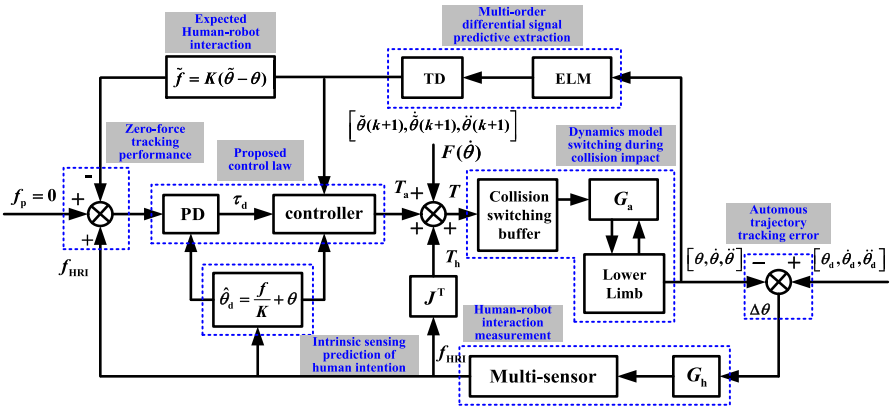

FIGURE 7. The intrinsic sensing prediction control strategy based on zero-force following principle.

where $s = \tilde{\theta} - \hat{\theta}_d$ is the deviation of the expected position of the exoskeleton and the human intented target trajectory, and the appropriate parameter matching of matrix K has influence on the proximity of $\tilde{\theta}$ and $\hat{\theta}_d$ and determines the following error of exoskeleton system.

The derivative of Lyapunov function is

$$\dot{V} = \frac{1}{2}\dot{s}^T\dot{M}(\tilde{\theta})\dot{s} + \dot{s}^T M(\tilde{\theta})\ddot{s} \tag{13}$$

According to the diagonal symmetry of the matrix $\dot{M}2C$ in the robotics, $\dot{s}^T\dot{M}\dot{s} = 2\dot{s}^T C\dot{s}$ and based on (10) and (11)

$$\begin{aligned}\dot{V} &= \dot{s}^T\left[M(\tilde{\theta})\ddot{s} + C(\tilde{\theta})\dot{s}\right] \\ &= -\dot{s}^T\left[M(\tilde{\theta})K_p K(\tilde{\theta} - \hat{\theta}_d) + M(\tilde{\theta})K_d K(\dot{\tilde{\theta}} - \dot{\hat{\theta}}_d)\right] \\ &= -\dot{s}^T M(\tilde{\theta})K_d K\dot{s} - \dot{s}^T M(\tilde{\theta})K_p K s \\ &= -\dot{s}^T M(\tilde{\theta})K_d K\dot{s} - \dot{s}^T w \end{aligned} \tag{14}$$

In (14), K_d, K, $M(\tilde{\theta})$ are positive definite matrices and are bounded when the exoskeleton moves in the finite motion range of joint angle. In order to eliminate the approximation deviation w, robust term $Wsgn(\dot{s})$ is introduce into the torque control law [42], $W = \text{diag}[w_{V_1}, w_{V_2}, \ldots, w_{V_n}]$, $w_{V_i} \geq |w_i|$, so as to ensure $\dot{V} \leq 0$.

Comparative experiments were conducted to control the exoskeleton to track human motion intention based on sensitivity amplification control (SAC), intrinsic sensing prediction control (ISPC), and intrinsic sensing prediction control with feedforward ELM compensation (ISPC_FEC). HRI force curves of the connecting rods of hip joint and knee joint are shown in Fig. 8. Due to the introduction of intrinsic sensing prediction and ELM feedforward compensation, the exoskeleton can track human intention flexibly and rapidly, which results in a substantial reduction of HRI and improvement of the system response. The HRI force dropped by 70.6% under the control strategy of ISPC_FEC during the swing phase trajectory, reducing the burden in the process of human-robot cooperative motion.

IV. LOCOMOTION STATE IDENTIFICATION WITH MULTI-SENSORS

A. GA_PSO-DNNS FOR LOCOMOTION MODE CLASSIFIER

To realize flexible follow-up of human motion intention under different terrains and gait motion trajectories, the system needs to intelligently recognize the locomotion mode of the current exoskeleton, and the control strategy and model parameters are effectively switched for the current corresponding motion mode. Based on the analysis and judgment of the internal sensor signals in the exoskeleton, intelligently autonomous control of the control system under unmanned intervention can be realized, thereby greatly improving the stability and flexibility of the exoskeleton system to adapt to different gait motion states. Based on the xPC-Target real-time kernel, the internal signals of sensors were transmitted from slave nodes to the master station via CANopen communication protocol, shown in the Fig. 9. Absolute encoders record the angle of each joints and the IMU6050 unit embedded in the back record the posture angles of the exoskeleton on itself, while GRF sensors and connecting rod sensors record the interaction force imposed by person on the exoskeleton.

As the wearable exoskeleton is a complex human-robot coupling system, the internal signals are generated under collaborative control and mainly include the angle, velocity and acceleration of each joint, back postures, IMU signals, plantar pressures, GRF forces, HRI forces and ZMP signals. Through filtering processing, extracted signals are stored as a row vector in a certain order

$$\mathrm{X} = [\theta_A, \xi_{IMU}, F_{pla}, F_{GRF}, F_{HRI}, \delta_{ZMP}] \tag{15}$$

The joint angles, back postures, plantar pressures and HRI forces are originally introduced, while the GRF forces are processed by weighted fusion according to the sensitivity of pressure region to ensure the response of each force sensor is easy to be detected, and the ZMP signals are fusioned through angles, velocity, acceleration of each joint and the mass property of lower limb exoskeleton. To ensure the iteration can converge quickly, the signals were pre-normalized

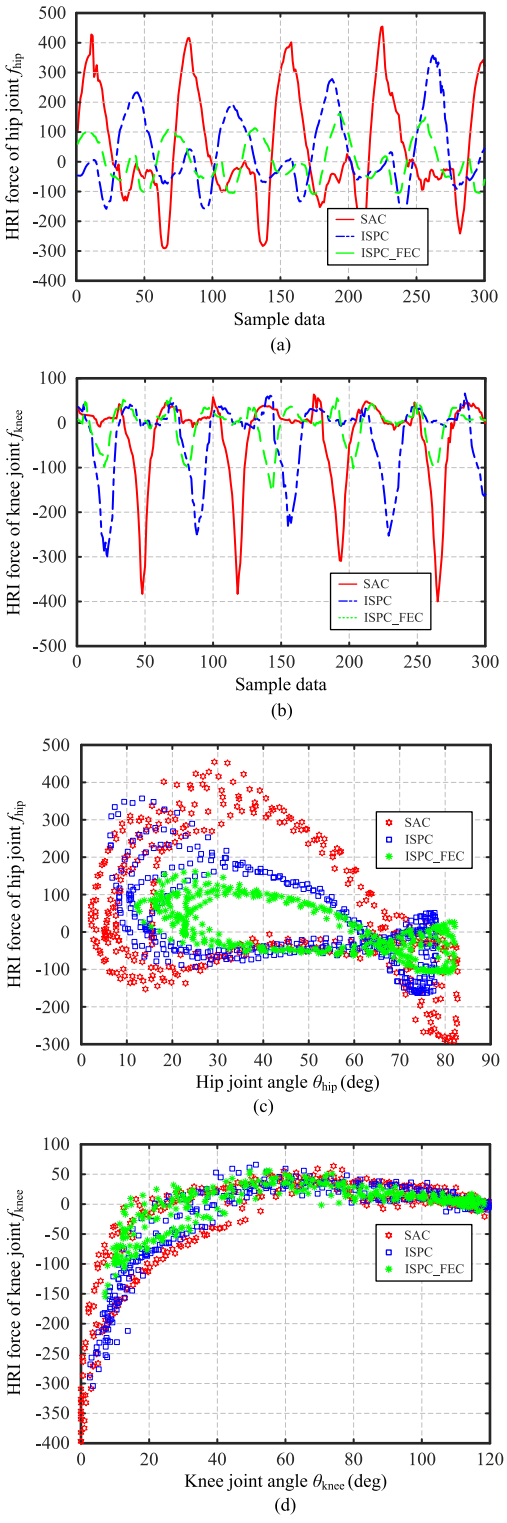

FIGURE 8. The HRI force during the trajectory tracking process.

before introduced into machine learning and deep learning algorithm. The identification accuracy often depends on sufficient feature extraction and signal stability. Therefore, the measured internal signals are appropriately filtered, and the first- and second-order differential forms of the above signals

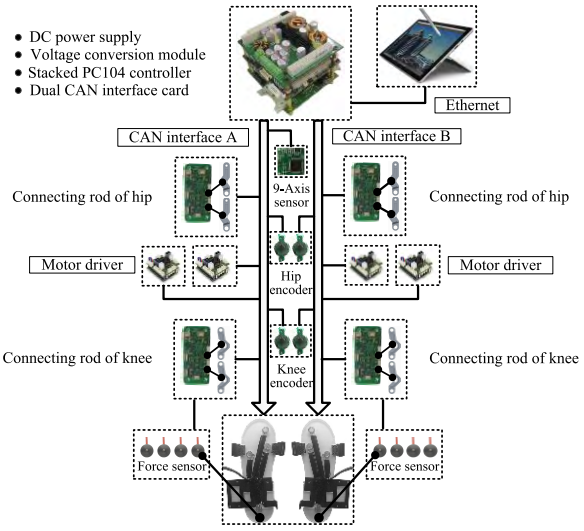

FIGURE 9. CAN bus based control architecture for the robotic exoskeleton.

are extracted to supplement the training samples, which are arranged in a certain order and stored in the form of vector $X \in R^{1\times 83}$. By extracting the signals in the past α moments and predicting the signals in the next γ moments, the internal sensor signals are packed into the following form:

$$\bar{X}|_{\alpha,\gamma} = [X^T_{k-\alpha}, \ldots, X^T_{k-1}, X^T_k, X^T_{k+1}, \ldots, X^T_{k+\gamma}] \quad (16)$$

A comparison experiment is conducted to analyze the identification results of the exoskeleton locomotion modes by machine learning and deep learning, as shown in TABLE 4. $\bar{X}|_{\alpha,\gamma=0} \in R^{9887\times 83}$ and $\bar{X}|_{\alpha=3,\gamma=1} \in R^{9887\times 415}$ are taken as the minimum feature samples and the maximum feature samples respected to sampling time respectively, to compare the identification accuracy, computing efficiency and the training period. Inside the feature samples, 6 locomotion modes from the processed data were gathered, including standing/transition (S/T), upstairs (W-S), downstairs (D-S), upramp (U-R), downramp (D-R), and walking (W).

For the machine learning algorithm, dimensional processing of the sample data by kernel principal component analysis (kPCA) is utilized to improve the feature extraction effect before introduced into the decision tree (DT), discriminant analysis (DA), support vector machine (SVM), k-nearest neighbor (KNN) and ensemble method (EM) for classification learning. Selecting an optimal feature set with the overall contribution rate of 95% by kPCA to reduce the dimensionality. Labeling the corresponding features set and training the models with 5-folds cross-validation method to find the optimal classifiers.

For the deep learning algorithm with strong feature extraction ability, the original collected data are directly input into the model for training and verification tests of deep neural networks (DNNs) and convolutional neural networks (CNNs). Reasonable parameter selection is beneficial to the training efficiency and accuracy of the identification models. To ensure the computing speed and the identification

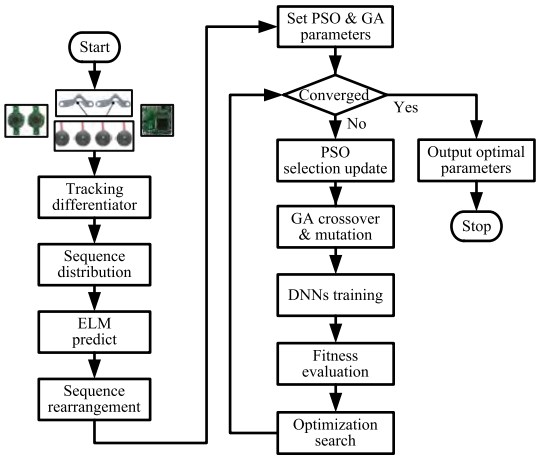

FIGURE 10. The search process of optimizing DNNs with GA_PSO.

accuracy, the dual-autoencoder DNNs model with 10 nodes on each layer and 4-Convolution-layer CNNs model solved by stochastic gradient descent with momentum are established. 75% of data samples are randomly selected to train the DNN network, and the remaining 25% of data samples are selected to verify the identification accuracy.

From the analysis of the results in the table, DA and DT have a shorter training period than SVM, KNN and EM, but the structures are relatively simple, and the overall identification accuracy is poor. Compared with that of the machine learning algorithm, the computation time of deep learning is reduced by at least 20 ms, the efficiency is improved by nearly 52%, and the data sets do not need to be additionally extracted by kPCA, which simplifies the complexity of the identification process and is suitable for the supplementary training of new signals to realize online updating of the model parameters. However, since the acquired data are converted into a two-dimensional matrix that has fewer rows and columns than the conventional image matrix, it is difficult to utilize the convolution kernel to fully scan the signal features for CNNs with appropriate parameters. Therefore, DNNs are proposed to identify the locomotion mode in this paper.

In DNNs, the increase of the levels result in the non-convex problems of objective optimization functions which depend on the initial value of the learning parameters, and the DNNs may be easily underfit with poor initialization. To avoid this uncertainty, we use the stacked autoencoders as our DNN model. In contrast to the other feedforward neural networks, the autoencoder is an unsupervised learning shallow neural network only focusing on the hidden layer and is typically utilized in data reduction and feature extraction. A stacked autoencoder DNN is a deep net combined of many autoencoders. Good parameters can be obtained with a stacked autoencoder if greedy-layer-wise training is used. The hybrid GA_PSO algorithm is introduced for searching optimal results. The optimization process of network parameters and the detailed algorithm of the GA_PSO-DNNs are shown in Fig. 10 and Table 3.

TABLE 3. GA_PSO optimization algorithm for DNNS.

Algorithm 1: GA_PSO search process of optimization for DNNs

Set *Maxgen*, *Popsize*, *Lenchrom*, *Parnum*, *Ctrlnum*, *Pc*, *Pm*;
  and other parameter definitions
Define parameter boundary *Bound*=[popmin, popmax;…;]
Initialize population *Pop*=popmax*rands(1, *Parnum*), velocity *Vel*=rands(1, *Parnum*)
Sort population sequence responding to index order
Calculate initial fitness
Select the best for global fitness *zbest* **and individual fitness** *gbest*
for *i*=1,2,...,*Maxgen* ***do***
 for *j*=1,2,...,*Popsize* ***do***
  V(*j*,:)+=c_1*rand*(*gbest*(*j*,:)-*Pop*(*j*,:))+ c_2*rand*(*zbest*-*Pop*(*j*,:))
  Pop(*j*,:)+= *w***Vel*(*j*,:)
  Cross, mutation and assign GA_Pop to PSO_Pop
  GA_Pop=*Cross*(*Pc*, *Lenchrom*, *Pop*, *Popsize*, *Bound*);
  GA_Pop=*Mutation*(*Pm*, *Lenchrom*, *GA_Pop*, *Popsize*, [*i Maxgen*], *Bound*);
  Pop=*GA_pop*;
  if *DNNsoptimization*(*Pop*(*j*,:))<0.005
   fitness(*j*)= *DNNsoptimization*(*Pop*(*j*,:))
  end
  update current optimal solution
 end
end

During iterative optimization process in Table 3, the speed and population are updated by PSO. Firstly, set the parameters for particle swarm optimization (PSO) and genetic algorithm (GA), define the boundary of the optimization parameters and initialize the particle velocity of the population to search for the initial global and individual optimal fitness of the chromosome. Then PSO population is transferred and operated through GA Cross and GA Mutation operation and finally transferred to PSO process for individual and global optimal update under the constraint conditions. In the iterative optimization process, the particle iteration speed is updated by [43]

$$V_{i,j}^{k+1} = w \cdot V_{i,j}^{k} + c_1 \cdot \alpha_{\mathrm{PSO}}(P_{\mathrm{gbest}}^{k} - P_{i,j}^{k}) + c_2 \cdot \beta_{\mathrm{PSO}}(P_{\mathrm{zbest}}^{k} - P_{i,j}^{k}) \quad (17)$$

where $V_{i,j}^{k+1}$ is the i-th particle's iteration speed at the $k+1$-th moment, w is the inertial weight for updating the iteration speed, c_1 and c_2 represent the searching ability for local and global optimization, respectively, α_{PSO} and β_{PSO} are random constant values, and P_{gbest}^{k} and P_{zbest}^{k} are the best fitness in the current iteration process among all particles.

Then, once the particle swarms have been crossed and mutated, the population and individual optimal fitness are updated under the constraint condition to perform the next iterative update of the optimal parameters. As the key parameters for raising the identification accuracy of the DNNs established in MATLAB, L2WeightRegularization, SparsityRegularization and SparsityProportion [44] for each

TABLE 4. Comparison of identification classifiers based on machine learning and deep learning.

Method	Index Type	Performance (Min/Max)	Accuracy (Min/Max)	Training (Min/Max)
DT	Gins diversity index	41.8 ms/53.2 ms	89.5 %/90.8 %	2.31 s/5.45 s
	Twoing rule	40.4 ms/55.3 ms	89.8 %/92.0 %	2.32 s/6.04 s
	Maximum deviance reduction	40.9 ms/53.9 ms	89.6 %/92.7 %	2.31 s/5.48 s
DA	Linear (diagonal covariance)	48.8 ms/52.1 ms	77.2 %/80.6 %	1.16 s/3.86 s
	Linear (full covariance)	43.2 ms/53.0 ms	82.6 %/86.5 %	1.29 s/3.96 s
	Quadratic (diagonal covariance)	43.9 ms/54.1 ms	78.8 %/80.6 %	1.21 s/3.92 s
	Quadratic (full covariance)	48.5 ms/55.2 ms	95.2 %/96.0 %	1.17 s/3.85 s
SVM	Linear kernel function	53.3 ms/59.0 ms	84.7 %/90.7 %	4.28 s/7.39 s
	Quadratic kernel function	63.3 ms/65.1 ms	91.1 %/95.1 %	4.68 s/7.46 s
	Cubic kernel function	59.8 ms/63.8 ms	93.7 %/96.3 %	4.78 s/7.37 s
	Gaussian kernel function	60.8 ms/68.1 ms	92.3 %/95.5 %	5.67 s/9.43 s
KNN	Euclidean metric	43.5 ms/58.4 ms	95.2 %/96.1 %	2.28 s/6.21 s
	Chebyshev metric	44.9 ms/56.7 ms	90.1 %/92.9 %	2.29 s/5.39 s
	Minkowski metric	52.4 ms/65.4 ms	94.3 %/96.8 %	37.79 s/61.52 s
	Mahalanobis metric	42.9 ms/67.8 ms	95.2 %/97.2 %	7.69 s/14.43 s
	Correlation metric	46.2 ms/63.4 ms	89.4 %/94.1 %	2.29 s/5.93 s
EM	Bag trees	68.6 ms/89.3 ms	91.8 %/91.9 %	7.73 s/11.44 s
	AdaBoost trees	69.5 ms/85.6 ms	89.0 %/91.2 %	27.23 s/47.72 s
	RUSBoost trees	72.4 ms/78.6 ms	82.1 %/92.9 %	15.33 s/27.45 s
	Subspace nearest neighbor	76.4 ms/94.9 ms	89.8 %/96.6 %	3.91 s/5.46 s
	Subspace discriminant	67.8 ms/133.5 ms	82.4 %/86.4 %	2.82 s/10.05 s
DNNs	2 Stacked autoencoders by unsupervised learning	37.6 ms/38.4 ms	97.2 %/97.3 %	3.04 s /5.26 s
CNNs	4-Convolution-layer structure solved by stochastic gradient descent with momentum	40.2 ms/45.5 ms	67.4 %/72.5 %	5.75 s /7.43 s

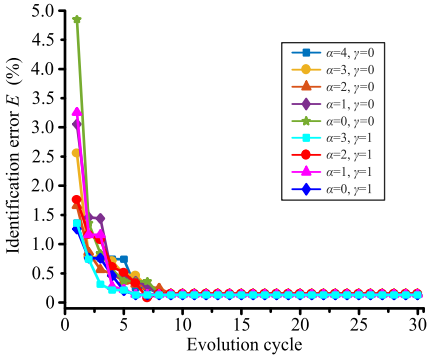

FIGURE 11. The optimization process of the identification error with evolution cycle. In the extracted signal form, α and γ are parameters of the composed sample data. α is the order of the former past moments, and γ is order of the predicted next moments.

autoencoder layer are optimized through the combination of GA and PSO. Taking the dual-autoencoder-DNNs with 10 nodes on each layer as an example, the optimization process of the identification accuracy rate with the evolution cycles is shown in Fig. 11. Taking the case $\bar{X}|_{\alpha=3,\gamma=1} \in R^{9887\times415}$ for analysis, the optimization process of the corresponding parameters for the DNNs is shown in Fig. 12.

After approximately 6 evolution cycles, the identification errors reach a minimum and remain approximately 0.2%, and the parameters of DNNs have searched for the optimal results. As shown in the Fig. 13, the identification accuracy of DNNs increases with the neuron nodes on each autoencoder layer, and the introduction of signals in the past few control cycles will greatly improve the identification accuracy as the value of α increases. However, as the network structure becomes more complex, the training effect and computing efficiency are greatly reduced. With GA_PSO algorithm optimization, the identification accuracy of the optimized network shown in Fig. 13 is generally between 99.2%–99.7%, and thus the accuracy is not constrained to the composition type of the sample data and the neuron nodes of the autoencoder layer. Fewer sample data extracted can also achieve accurate identification with higher accuracy, which greatly reduces the computing load and running time of nodes in the network.

The confusion matrix is usually used to visualize the performance of the learning algorithm on each class. It is essentially a specific table layout, also called error matrix. Each row of the matrix represents the instances in a predicted class, while each column represents the instances in an actual class. In our research, we aim to classify 6 locomotion modes, including S/T, W-S, D-S, U-R, D-R, and W. The confusion matrices before optimization and after optimization are shown in TABLE 5 and 6.

For example, the first element in row D-S and column S/T indicates the number of real S/T state test data predicted to be in the D-S state, and the second element below that indicates the percentage it takes. The first element in PPV represents the precision or positive predictive value, which indicates the percentage of correct predictions among all same predictions. The first element in TPR represents sensitivity or true positive rate, which indicates percentage of correct predictions among

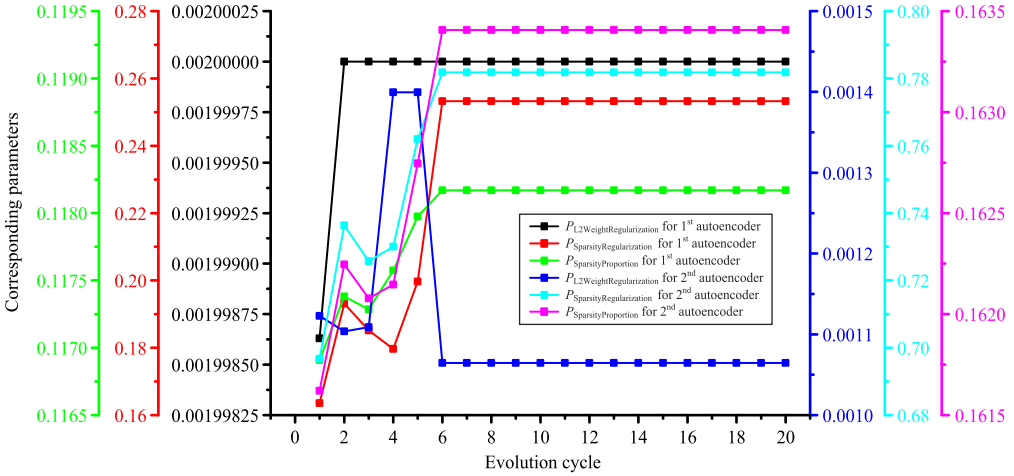

FIGURE 12. The optimization process of the corresponding parameters of DNNs through the combination of GA and PSO.

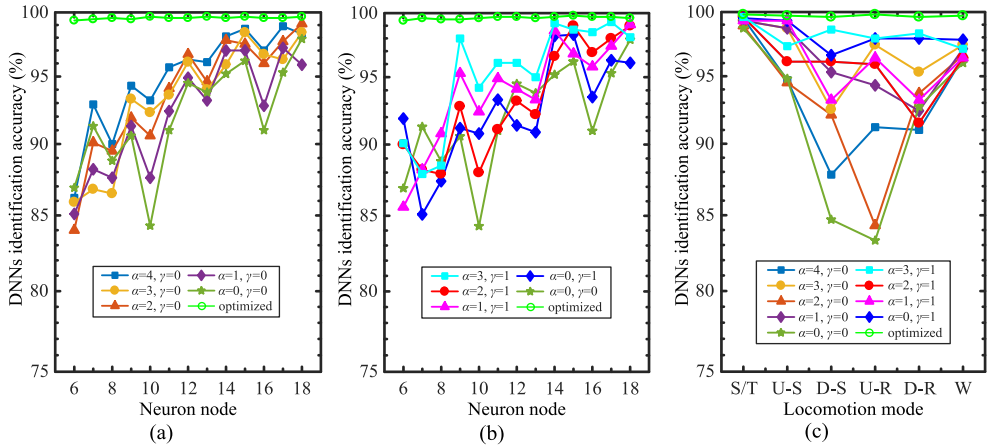

FIGURE 13. The DNNs identification accuracy with GA_PSO optimization. In the extracted signal form, α and γ are parameters of the composed sample data. α is the order of the former past moments, and γ is order of the predicted next moments.

TABLE 5. Confusion matrix for identification results of the DNNS classifier without GA_PSO.

	S/T	U-S	D-S	U-R	D-R	W	PPV
S/T	**1457**	0	2	2	7	3	99.0%
	59.0%	0.0%	0.1%	0.1%	0.3%	0.1%	1.0%
U-S	0	**140**	0	1	0	0	99.3%
	0.0%	**5.7%**	0.0%	0.0%	0.0%	0.0%	0.7%
D-S	6	0	**141**	0	8	0	91.0%
	0.2%	0.0%	**5.7%**	0.0%	0.3%	0.0%	9.0%
U-R	5	7	0	**185**	0	2	93.0%
	0.2%	0.3%	0.0%	**7.5%**	0.0%	0.1%	7.0%
D-R	7	0	4	0	**209**	5	92.9%
	0.3%	0.0%	0.2%	0.2%	**8.5%**	0.2%	7.1%
W	0	0	0	4	10	**266**	95.0%
	0.0%	0.0%	0.0%	0.2%	0.4%	**10.8%**	5.0%
TPR	98.8%	95.2%	95.9%	96.4%	89.3%	96.4%	97.2%
	1.2%	4.8%	4.1%	3.6%	10.7%	3.6%	2.8%

TABLE 6. Confusion matrix for identification results of the GA_PSO-DNNS classifier.

	S/T	U-S	D-S	U-R	D-R	W	PPV
S/T	**1469**	0	0	0	0	3	99.8%
	59.4%	0.0%	0.0%	0.0%	0.0%	0.1%	0.2%
U-S	0	**147**	0	0	0	0	99.9%
	0.0%	**5.9%**	0.0%	0.0%	0.0%	0.0%	0.1%
D-S	1	0	**147**	0	1	0	98.7%
	0.1%	0.0%	**5.9%**	0.0%	0.0%	0.0%	1.3%
U-R	1	0	0	**191**	0	0	99.5%
	0.0%	0.0%	0.0%	**7.7%**	0.0%	0.0%	0.5%
D-R	1	0	0	1	**233**	0	99.1%
	0.0%	0.0%	0.0%	0.0%	**9.4%**	0.0%	0.9%
W	3	0	0	0	0	**273**	98.9%
	0.1%	0.0%	0.0%	0.0%	0.0%	**11.0%**	1.1%
TPR	99.6%	99.9%	99.8%	99.5%	99.6%	98.9%	99.7%
	0.4%	0.1%	0.2%	0.5%	0.4%	1.1%	0.3%

all same actual states. The second element in these two classes indicates loss.

In the dual-autoencoder-DNNs with 10 nodes on each layer, the input extracted signal vector entering the DNNs is $X \in R^{1\times 83}$and the out identified label vector is $L_{\text{mode}} = [l_{\text{S/T}}, l_{\text{U-S}}, l_{\text{D-S}}, l_{\text{U-R}}, l_{\text{D-R}}, l_{\text{W}}] \in R^{1\times 6}$. Identified label for each locomotion mode is ranged from 0 to 1, and the algebra

sum of identified labels for 6 locomotion modes always maintains 1. To reasonably judge the current locomotion mode, the identified label for U-S, D-S, U-R, D-R and W should reach above 0.9 in 5 consecutive sampling periods. Otherwise it is considered to be identified as S/T mode for safety. The confusion matrix of DNNs with GA_PSO algorithm optimization is analyzed. The overall accuracy rate is improved from 97.2% to 99.7%, and the accuracy of each classification label is basically maintained at approximately 99%, thus realizing accurate identification of each locomotion mode.

B. ANFIS FOR GAIT PHASE CLASSIFIER

The Tagaki-Sugeno fuzzy inference engine supports simplifying the output of rules into a linear combination or constant value of input variables that is suitable for mathematical analysis. The neural network can effectively and directly learn from the samples, providing advantages of distributed information storage, parallel computing, and high fault tolerance. Therefore, ANFIS constructed by the combination of the above two sections has strong adaptive learning ability. Therefore, the data fusion and analysis of the plantar pressure signals are performed by the ANFIS model, and the obtained identification result is not strictly 0 or 1 but the probability relative to the two phases in the form of continuous values between [0, 1]. In addition, the trained model has high identification accuracy for the data that have not been trained, thus indicating strong generalization ability.

The antecedent network of the Tagaki-Sugeno ANFIS is divided into an input layer, fuzzification layer, fuzzy rule calculation layer and normalization layer. The fuzzy rule calculation layer in the antecedent network multiplies the membership value of the fuzzified input variables to obtain the fitness of each fuzzy rule by

$$\alpha_j = \mu_{A_1^j}(x_1) \wedge \mu_{A_2^j}(x_2) \cdots \wedge \mu_{A_n^j}(x_n) \tag{18}$$

The normalization layer has the same number of nodes as the third layer to normalize the fitness value for the next step to calculate the output in the consequent network. The consequent network is divided into an input layer and a consequent rule calculation layer. Each node of the second layer in the consequent network represents a rule that is the normalized usage of the fuzzy rules and is multiplied by output nodes in the antecedent network as the connecting weight to calculate the weighted summation expressed as

$$z = \sum_{j=1}^{m} \bar{\alpha}_j y_j \tag{19}$$

where $\bar{\alpha}_j$ is the output of j-th node in the antecedent network, and y_j is the normalized usage of the fuzzy rules.

The weighted summation of the four plantar sensor pressures is calculated, and its first-order and second-order differential signals are also extracted as input samples for import into the ANFIS. Introducing speed and acceleration can accurately reflect the true force response, contact impact and gait change frequency in the process of contact between the sole and the ground. The domain is divided into three fuzzy sets of low, medium and high by the initially set trapezoidal membership function.

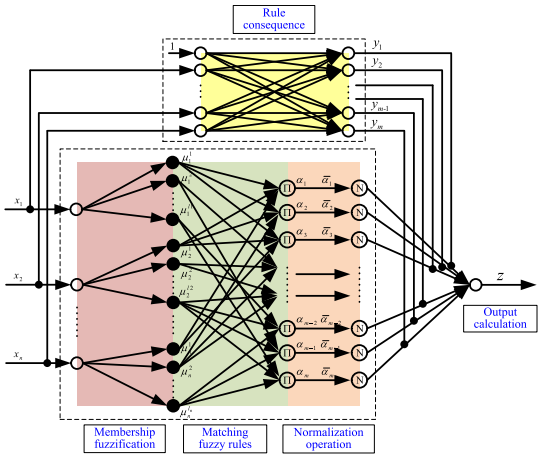

FIGURE 14. The simplified structure diagram of ANFIS.

The fuzzy-neural network generally takes 1800 sets of input samples to optimize 63 adjustable parameters (36 membership function parameters for 3 input nodes & 27 connection weights for each output node) and verify the classification accuracy. As the training data, 1000 sets of samples are randomly extracted, and the remaining 800 samples are used as the post-training validation data. The iteration is terminated after 3000 learning epochs, during which the calculation error decreases from 3.7%–8.5% to 0.5%–0.7%, which is much closer to the initial iteration error $\eta = 1e^{-6}$. The optimized membership functions and the output label of gait phase for the locomotion modes of W, U-S, D-S, U-R, and D-R are shown in Fig. 15 and Fig. 16. The predictive label of the gait phase under certain conditions is not absolutely equal to 0 (swing phase) or 1 (stance phase), and the identified label value fluctuates in the adjacent domain of the demanded label value. For untrained sampled occasions, ANFIS gait phase identification still works properly with high precision, thus laying a great foundation for the switching of the corresponding control strategy during the swing phase and stance phase.

C. PROTOTYPE AND EXPERIMENT

To evaluate the performance of the proposed control strategy under the corresponding locomotion state identification, experiments for the gait motions of W, U-S, D-S, U-R, and D-R were carried out as shown in Fig. 17. Under the proposed strategy based on ISPC and locomotion state identification with multi-sensor, the extracted ZMP signals calculated by (20) of the human-exoskeleton system carrying 30kg-weighted load are similar to those obtained when the wearer moves without the exoskeleton. Based on the GA_PSO optimized DNNs and ANFIS, corresponding control parameters and gait phase classifiers can be switched naturally under the gait motions of W, U-S, D-S, U-R, and D-R to achieve

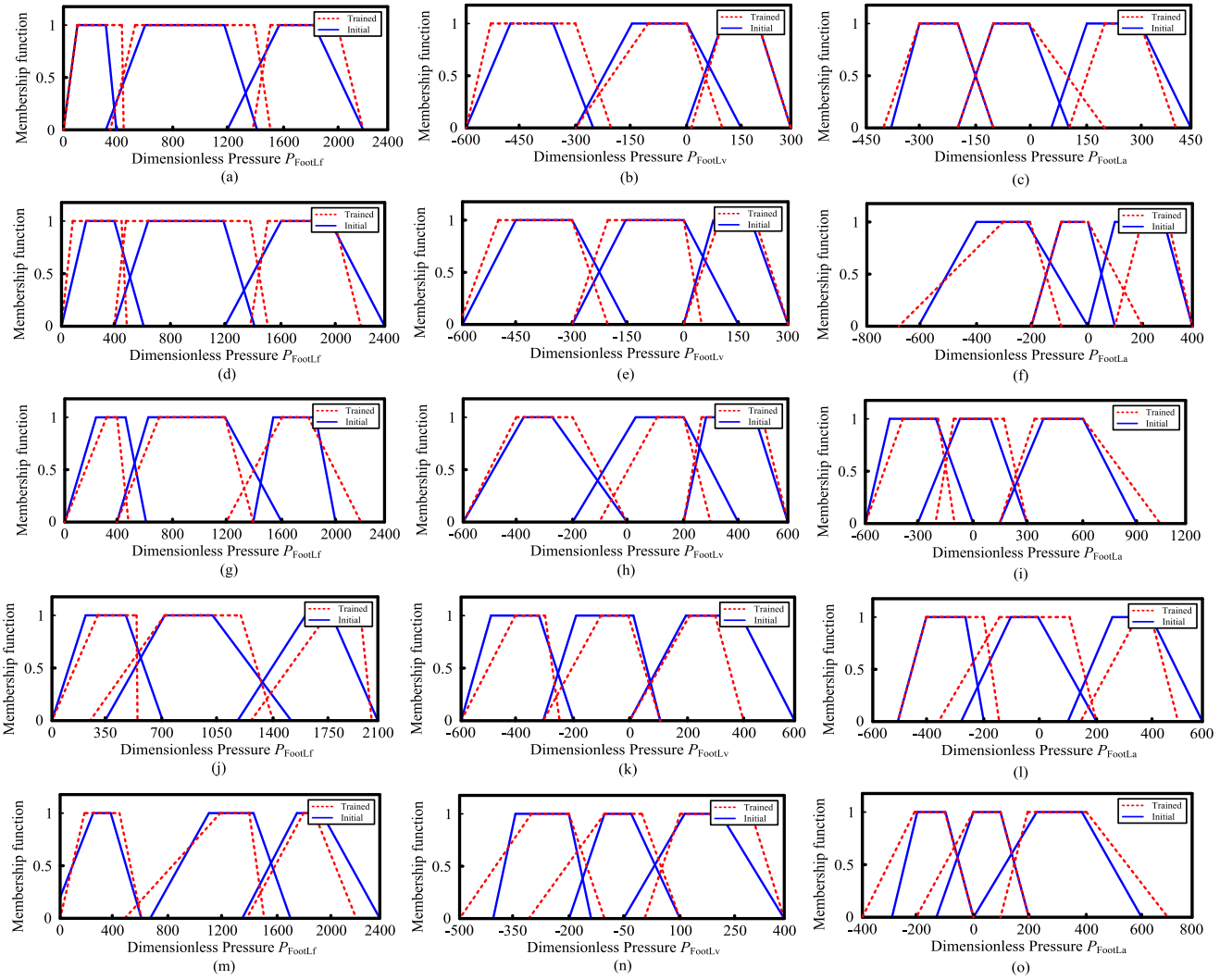

FIGURE 15. The ANFIS membership function curves under W, U-S, D-S, U-R, and D-R.

accurate locomotion mode identification, gait phase switching, human intention prediction and flexible follow-up.

$$\begin{cases} X_{\mathrm{ZMP}} = \dfrac{\sum_{i=1}^{n} m_i(\ddot{Z}_i + g)X_i - \sum_{i=1}^{n} m_i\ddot{X}_i Z_i}{\sum_{i=1}^{n} m_i(\ddot{Z}_i + g)} \\ Y_{\mathrm{ZMP}} = \dfrac{\sum_{i=1}^{n} m_i(\ddot{Z}_i + g)Y_i - \sum_{i=1}^{n} m_i\ddot{Y}_i Z_i}{\sum_{i=1}^{n} m_i(\ddot{Z}_i + g)} \end{cases} \tag{20}$$

where X, Y, Z, and m_i are the positions and mass quality of each part of the exoskeleton in the base coordinate system.

ZMP trajectories can evaluate the balance holding capacity of the human-exoskeleton system. It can be seen from Fig. 18 that ZMP signals can maintain stable in the small range during 5 gait trajectories, which is much similar to the ZMP of human without wearing the exoskeleton.

The pressure curves of the GRF sensors inside the shoes during the process of carrying heavy load with exoskeleton was extracted and analyzed, as shown in the Fig. 19. Although the average of GRF sensors during gait motions increases about 8% due to impact contact with ground, the trend and range of value curves remain the same and the exoskeleton can bear the load for human body.

The HRI force signals on hip and knee joint sensors during 5 motion trajectories were extracted for evaluating tracking effect by

$$RMSE = \sqrt{\sum_{i=1}^{N} \|F_{\mathrm{HRI}}\|^2 / N} \tag{21}$$

The tracking effect is evaluated by comparative analysis on the root mean square error (RMSE) of HRI

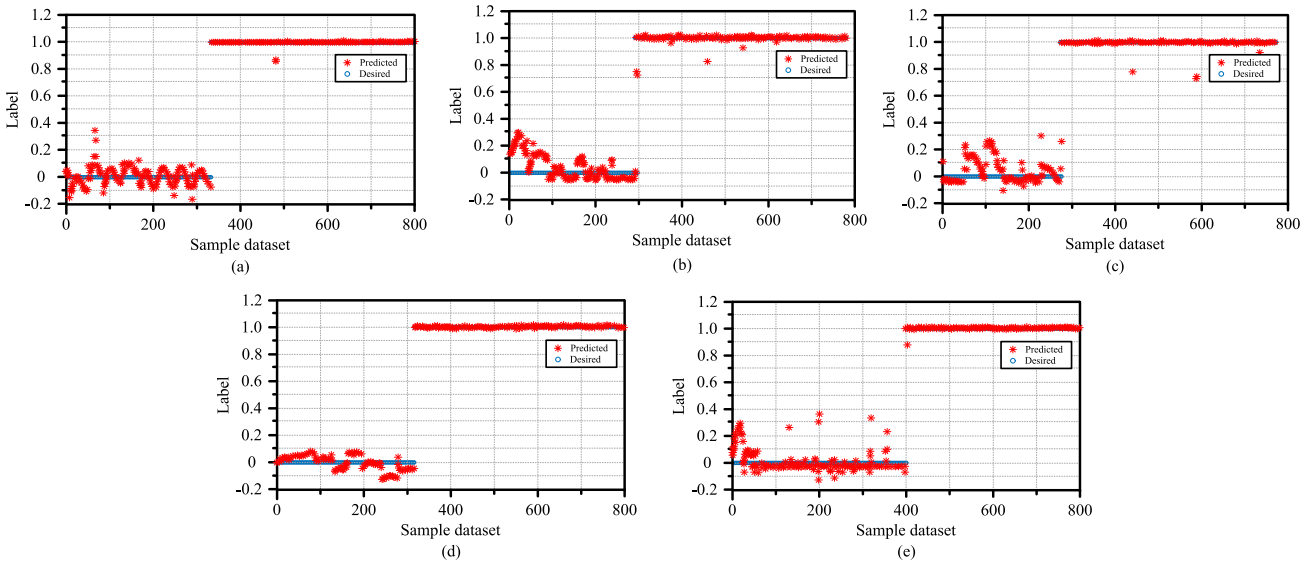

FIGURE 16. The verification of generalization ability for ANFIS under W, U-S, D-S, U-R, and D-R.

FIGURE 17. Experimental research of the human-exoskeleton system under the proposed strategy during W, U-S, D-S, U-R, and D-R.

TABLE 7. Tracking effect for HIP joint.

Gait	HRI without load carrying	HRI under load carrying
W	112.63	126.84
U-S	124.21	140.85
D-S	152.12	183.83
U-R	111.72	130.76
D-R	135.36	156.15

TABLE 8. Tracking effect for knee joint.

Gait	HRI without load carrying	HRI under load carrying
W	210.49	238.24
U-S	174.37	198.66
D-S	172.28	203.37
U-R	206.11	233.14
D-R	222.56	250.25

force, as shown in the following table 7 and table 8. The RMSE value collected under load carrying condition rises only about 12.6%–17.1% than that without load carrying.

According to [25], to evaluate the conversion efficiency between locomotion modes, define the identification delay of conversion process

$$T_{\mathrm{ID}} = \frac{T_{\mathrm{I}} - T_{\mathrm{C}}}{T_{\mathrm{gait}}} \times 100\% \tag{22}$$

where T_{gait} is the duration of the gait cycle, T_{C} is the critical time, T_{I} is the moment when the locomotion mode transition is identified correctly for the first time. Taking gait conversion from W to U-R and U-R to W as example, the angle curve of

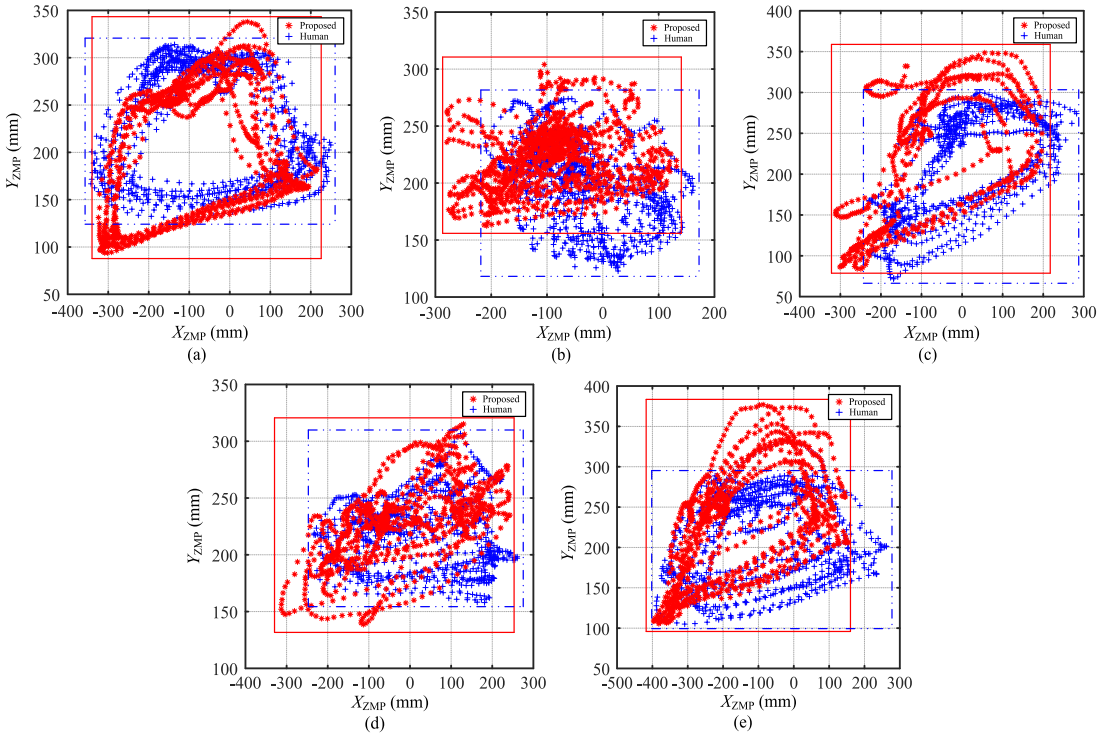

FIGURE 18. ZMP signals of the exoskeleton system under W, U-S, D-S, U-R, and D-R.

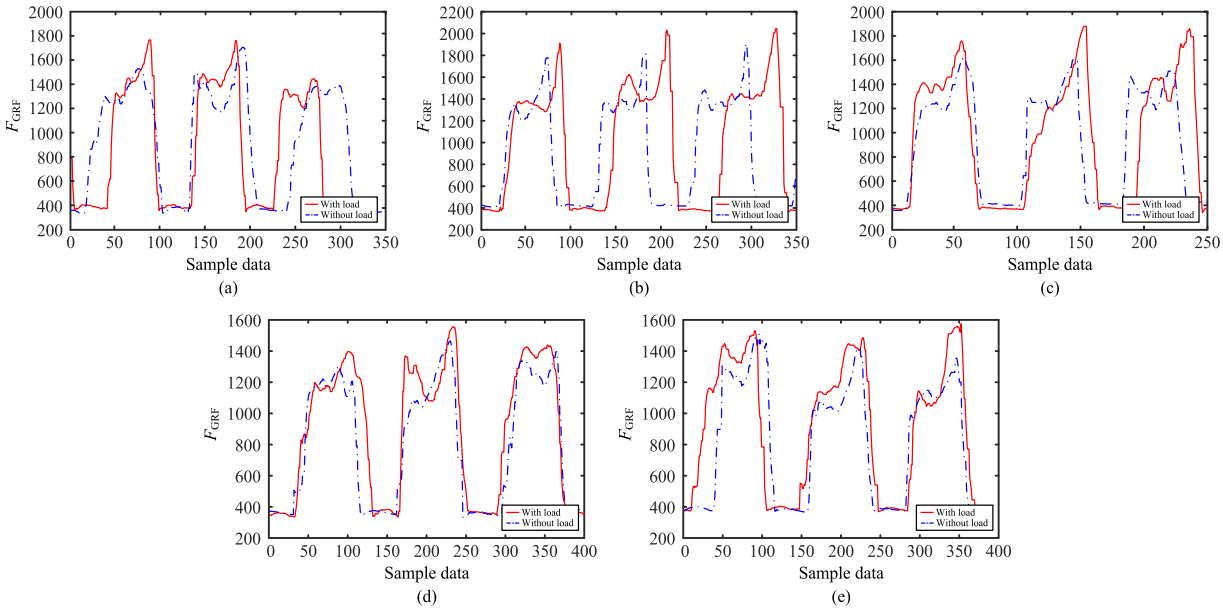

FIGURE 19. GRF sensor signals of the exoskeleton system under W, U-S, D-S, U-R, and D-R.

hip joint and the identification label were drawn in Fig. 20 to explain the conversion process.

The identification conversion efficiency depends on the generalization ability for untrained sample cases. In order to improve the conversion efficiency, the gait transition in the conversion process and the label categories need to be refined in the future research work to further enhance the identification conversion efficiency.

To evaluate the human physiological reaction to the assistance of exoskeleton, heart rate characteristics of consecutive operation under load carrying during W, U-S, D-S, U-R, and D-R gait trajectories were recorded. The average heart rate of

TABLE 9. Conversion time of identification delay.

Conversion type	Identification delay
W to U-S	16.5% ± 1.8%
U-S to W	16.4% ± 1.1%
W to D-S	16.3% ± 2.3%
D-S to W	11.8 %± 0.9%
W to U-R	15.2% ± 3.5%
U-R to W	13.8% ± 2.8%
W to D-R	17.4% ± 1.2%
D-R to W	12.7 %± 3.0%

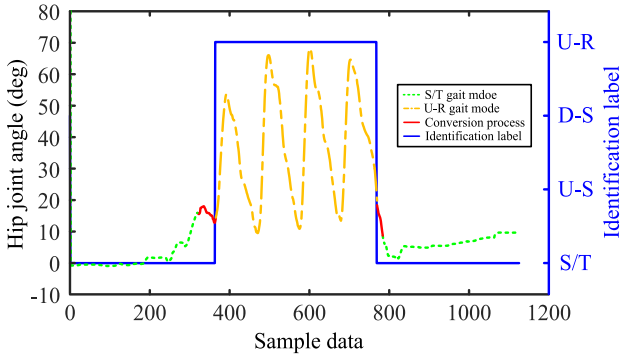

FIGURE 20. Conversion process from W to U-R and U-R to W.

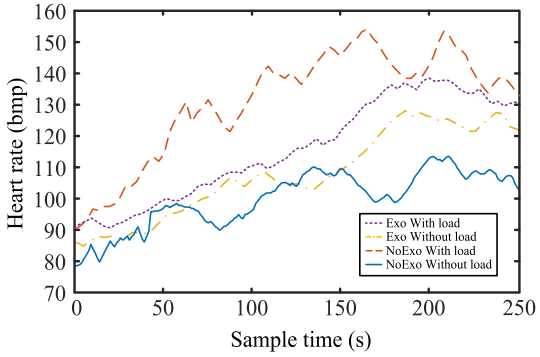

FIGURE 21. Heart rate signals of the wear under consecutive operation during W, U-S, D-S, U-R, and D-R.

the wearer is shown in Fig. 21. Compared with NoExo without load, the heart rate of NoExo with load rises about 40.3% during the five consecutive trajectories, while the heart rate of Exo with and without load rises only 21.3% and 17.5%, proving the effective assistance of the proposed exoskeleton system.

V. CONCLUSION

A novel lower limb exoskeleton actuated by a variable magnification ratio structure is proposed in this paper. With optimized hanging point positions and size parameters, the output torque of active hip and knee joints can fully envelope the demand load area under a 55-kg-weight-lifting condition. The overall weight of the exoskeleton prototype is minimized to 22.5 kg, and the reduction ratio of the actuator is reduced from 6 to 3.5, which greatly improves the flexibility and portability of the exoskeleton. A newly developed split embedded intrinsic sensor can accurately measure the HRI force applied to the exoskeleton and extract the human motion intention without being affected by differences in wearing status. Based on the ISPC with feedforward ELM compensation, the HRI force drops by 70.6% compared with that of the SAC strategy, substantially reducing the burden in the process of human-robot cooperative motion. To choose an efficient identification classifier, comparative experiments were carried out to analyze the identification efficiency and computation load of machine learning and deep learning. With the optimized GA_PSO algorithm, the identification accuracy of the DNNs is enhanced from 97.2% to 99.7%. To flexibly switch between the stance phase and swing phase, the corresponding ANFIS model is introduced to classify the gait phase under each locomotion mode. The predictive label of the gait phase under untrained occasions fluctuates in the adjacent domain of the demanded label value 0 (swing phase) and 1 (stance phase), showing great generalization ability. Experiments under the gait motions of W, U-S, D-S, U-R, and D-R are performed, and the performance for human intention tracking is improved under the proposed control strategy assisted with the corresponding locomotion state identification.

The novel structure and control strategy proposed in this paper can well assist wearer, which guarantee the flexibility and portability of the exoskeleton system under heavy-load-carrying conditions. Based on the current theoretical results, we will continue to research the efficient autunomous control strategy for flexiable tracking. In order to further improve the prediction of human motion intention, the establishment of more complex impedance model for HRI force will be taken into account. For reducing the HRI during motion tracking process, precise modeling of dynamics of human-robot coupling system will be considered by introducing the online parametric system identification techniques. We will analyze and discuss these issues in the future work to enhance the adaptability of the exoskeleton to various tasks and conditions.

REFERENCES

[1] A. M. Dollar and H. Herr, "Lower extremity exoskeletons and active orthoses: Challenges and state-of-the-art," *IEEE Trans. Robot.*, vol. 24, no. 1, pp. 144–158, Feb. 2008.
[2] W. Meng, Q. Liu, Z. D. Zhou, Q. S. Ai, B. Sheng, and S. Q. Xie, "Recent development of mechanisms and control strategies for robot-assisted lower limb rehabilitation," *Mechatronics*, vol. 31, pp. 132–145, Oct. 2015.
[3] T. F. Yan, M. Cempini, C. M. Oddo, and N. Vitiello, "Review of assistive strategies in powered lower-limb orthoses and exoskeletons," *Robot. Auto. Syst.*, vol. 64, pp. 120–136, Feb. 2015.
[4] A. B. Zoss, H. Kazerooni, and A. Chu, "Biomechanical design of the Berkeley lower extremity exoskeleton (BLEEX)," *IEEE/ASME Trans. Mechatronics*, vol. 11, no. 2, pp. 128–138, Apr. 2006.
[5] R. Bogue, "Exoskeletons and robotic prosthetics: A review of recent developments," *Ind. Robot, A Int. J.*, vol. 36, no. 5, pp. 421–427, 2009.
[6] S. Karlin, "Raiding iron Man's closet [geek life]," *IEEE Spectr.*, vol. 48, no. 8, p. 25, Aug. 2011.
[7] K. Yamamoto, K. Hyodo, M. Ishii, and T. Matsuo, "Development of power assisting suit for assisting nurse labor," *JSME Int. J. Ser.*, vol. 46, no. 3, pp. 703–711, 2002.

[8] S. Toyama and G. Yamamoto, "Development of Wearable-Agri-Robot mechanism for agricultural work," in *Proc. IEEE/RSJ Int. Conf. Intell. Robot. Syst.*, Oct. 2009, pp. 5801–5806.

[9] A. Tsukahara, R. Kawanishi, Y. Hasegawa, and Y. Sankai, "Sit-to-stand and stand-to-sit transfer support for complete paraplegic patients with robot suit HAL," *Adv. Robot.*, vol. 24, no. 11, pp. 1615–1638, 2010.

[10] *RB3D*. Paris, France. Accessed: Jun. 2015. [Online]. Available: https://www.rb3d.com/wp-content/uploads/2015/06/RB3D_Brochure EXO_HV3_EN_L.pdf

[11] S. Chen *et al.*, "Adaptive robust cascade force control of 1-DOF hydraulic exoskeleton for human performance augmentation," *IEEE/ASME Trans. Mechatronics*, vol. 22, no. 2, pp. 589–600, Apr. 2017.

[12] X. Ouyang, S. Ding, B. Fan, P. Y. Li, and H. Yang, "Development of a novel compact hydraulic power unit for the exoskeleton robot," *Mechatronics*, vol. 38, pp. 68–75, Sep. 2016.

[13] S. Chen, Z. Chen, and B. Yao, "Precision cascade force control of multi-DOF hydraulic leg exoskeleton," *IEEE Access*, vol. 6, pp. 8574–8583, 2018.

[14] J. X. Cui, Y. H. Zhu, and B. Z. Xu, "Virtual coupling based control methodology for lower extremity exoskeleton," *Appl. Mech. Mater.*, vols. 556–562, pp. 2365–2369, May 2014.

[15] Y. H. Zhu, J. X. Cui, and J. Zhao, "Biomimetic design and biomechanical simulation of a 15-DOF lower extremity exoskeleton," in *Proc. IEEE Int. Conf. Robot. Biomimetics*, Dec. 2013, pp. 1119–1124.

[16] Y. H. Zhu, G. A. Zhang, C. Zhang, G. F. Liu, and J. Zhao, "Biomechanical modeling and load-carrying simulation of lower limb exoskeleton," *Bio-Med. Mater. Eng.*, vol. 26, no. 1, pp. S729–S738, 2015.

[17] Z. O. Khokhar, Z. G. Xiao, and C. Menon, "Surface EMG pattern recognition for real-time control of a wrist exoskeleton," *Biomed. Eng. Online*, vol. 9, no. 1, p. 41, 2010.

[18] T. Lenzi, S. M. M. De Rossi, N. Vitiello, and M. C. Carrozza, "Intention-based EMG control for powered exoskeletons," *IEEE Rev. Biomed. Eng.*, vol. 59, no. 8, pp. 2180–2190, Aug. 2012.

[19] J. Gancet *et al.*, "MINDWALKER: Going one step further with assistive lower limbs exoskeleton for SCI condition subjects," in *Proc. IEEE 4th IEEE RAS EMBS Int. Conf. Biomed. Robot. Biomechatronics*, vol. 49, Jun. 2012, pp. 1794–1800.

[20] J. F. Veneman, R. Kruidhof, E. E. G. Hekman, R. Ekkelenkamp, E. H. F. V. Asseldonk, and H. V. D. Kooij, "Design and evaluation of the LOPES exoskeleton robot for interactive gait rehabilitation," *IEEE Trans. Neural Syst. Rehabil. Eng.*, vol. 15, no. 3, pp. 379–386, Sep. 2007.

[21] C. Zhang, X. Z. Zang, Z. F. Leng, H. Y. Yu, J. Zhao, and Y. H. Zhu, "Human-machine force interaction design and control for the hit load-carrying exoskeleton," *Adv. Mech. Eng.*, vol. 8, no. 4, 2016. Art no. 16878140.

[22] L. K. Wang, Z. J. Du, W. Dong, Y. Shen, and G. Y. Zhao, "Intrinsic sensing and evolving internal model control of compact elastic module for a lower extremity exoskeleton," *Sensors*, vol. 18, no. 3, p. 909, 2018.

[23] K. Kora, C. Z. Lu, and A. J. Mcdaid, "Automatic tuning with feedforward compensation of the HuREx rehabilitation system," in *Proc. IEEE/ASME Int. Conf. Adv. Intell. Mechatronics*, Jul. 2014, pp. 1504–1509.

[24] Y. Marzieh, K. Alireza, G. Reza, and S. Pouria, "Combined neural network Feedforward and RISE feedback control structure for a 5 DOF upper-limb exoskeleton robot with asymptotic tracking," *J. Adv. Comput. Res.*, vol. 6, no. 1, pp. 47–62, 2015.

[25] H. Chen, J. Zhang, X. G. Zhang, and Y. H. Hu, "A robust-elm approach based on parzen windiow's estimation for kiln sintering temperature detection," *Acta AutomaticSinica*, vol. 38, no. 5, pp. 841–849, 2012.

[26] K. Yuan, Q. Wang, and L. Wang, "Fuzzy-logic-based terrain identification with multisensor fusion for transtibial amputees," *IEEE/ASME Trans. Mechatronics*, vol. 20, no. 2, pp. 618–630, Apr. 2015.

[27] Y. Long *et al.*, "PSO-SVM-based online locomotion mode identification for rehabilitation robotic exoskeletons," *Sensors*, vol. 16, no. 9, p. 1408, 2016.

[28] N. S. Kwak, K. R. Müller, and S. W. Lee, "A convolutional neural network for steady state visual evoked potential classification under ambulatory environment," *PLoS One*, vol. 12, no. 2, 2017, Art. no. 0172578.

[29] C. Meng and X. Zhao, "Webcam-based eye movement analysis using CNN," *IEEE Access*, vol. 5, pp. 19581–19587, 2017.

[30] H. Yu, Z. H. Tan, Y. Zhang, Z. Ma, and J. Guo, "DNN filter bank cepstral coefficients for spoofing detection," *IEEE Access*, vol. 5, pp. 4779–4787, 2017.

[31] Y. Saito, S. Takamichi, and H. Saruwatari, "Training algorithm to deceive anti-spoofing verification for DNN-based speech synthesis," in *Proc. IEEE Int. Conf. Acoust., Speech Signal Process.*, Mar. 2017, pp. 4900–4904.

[32] T. Wang, X. Ye, L. Wang, and H. Li, "Grid search optimized SVM method for dish-like underwater robot attitude prediction," in *Proc. 15th Int. Joint Conf. Comput. Sci. Optim.*, Jun. 2012, pp. 839–843.

[33] H. Karimi, F. Yousefi, and M. R. Rahimi, "Correlation of viscosity in nanofluids using genetic algorithm-neural network (GA-NN)," *Heat Mass Transfer*, vol. 47, no. 11, pp. 1417–1425, 2011.

[34] F. Ye, "Particle swarm optimization-based automatic parameter selection for deep neural networks and its applications in large-scale and high-dimensional data," *PLos One*, vol. 12, no. 12, 2017, Art no. 0188746.

[35] D. Sharma, P. Gaur, and A. P. Mittal, "Comparative analysis of hybrid GAPSO optimization technique with GA and PSO methods for cost optimization of an off-grid hybrid energy system," *Energy Technol. Policy*, vol. 1, no. 1, pp. 106–114, 2014.

[36] P. Ghamisi, "A novel method for segmentation of remote sensing images based on hybrid GAPSO," *Int. J. Comput. Appl.*, vol. 29, no. 2, pp. 7–14, 2013.

[37] B. Chen, X. Wang, Y. Huang, K. Wei, and Q. Wang, "A foot-wearable interface for locomotion mode recognition based on discrete contact force distribution," *Mechatronics*, vol. 32, pp. 12–21, Dec. 2015.

[38] T. Anwar and A. A. Jumaily, "System identification and damping coefficient estimation from EMG based on ANFIS to optimize human exoskeleton interaction," in *Proc. IEEE Int. Conf. Fuzzy Syst.*, Jul. 2016, pp. 844–849.

[39] A. S. Ghafari, A. Meghdari, and G. R. Vossoughi, "Intelligent control of powered exoskeleton to assist paraplegic patients mobility using hybrid neuro-fuzzy ANFIS approach," in *Proc. IEEE Int. Conf. Robot. Biomimetics*, Dec. 2006, pp. 733–738.

[40] L. Q. Wu, H. Lin, and J. Q. Han, "Study of tracking differentiator on filtering," *Acta Simulata Systematica Sinica*, vol. 16, no. 4, pp. 636–651, 2004.

[41] G. B. Huang, Q. Y. Zhu, and C. K. Siew, "Extreme learning machine: Theory and applications," *Neurocomputing*, vol. 70, pp. 489–501, Dec. 2006.

[42] J. K. Liu, "Charpter 4 Fuzzy adaptive control for robot arm," in *Robot Control System Design Matlab Simulation-Basic Design Method*, 1st ed. Beijing, China: Univ. Tsinghua Press, 2016, pp. 77–78.

[43] M. Sheikhalishahi, V. Ebrahimipour, H. Shiri, H. Zaman, and M. Jeihoonian, "A hybrid GA-PSO approach for reliability optimization in redundancy allocation problem," *Int. J. Adv. Manuf. Technol.*, vol. 68, pp. 317–338, Sep. 2013.

[44] *Train Stacked Autoencoders for Image Classification* The MathWorks. Natick, Massachusetts, USA. [Online]. Available: https://ww2.mathworks.cn/help/deeplearning/examples/train-stacked-autoencoders-for-image-classification.html

YUXIANG HUA received the B.S. degree in mechanical engineering and the M.S. degree in aerospace manufacturing engineering from the Harbin Institute of Technology (HIT), Harbin, China, in 2015 and 2017, respectively, where he is currently pursuing the Ph.D. degree with the School of Mechatronics Engineering.

His research interests include adaptive control strategy, wearable rehabilitation robots, and robotic exoskeleton.

JIZHUANG FAN received the B.S. degree in mechatronics engineering from the Harbin University of Science and Technology, Harbin, China, in 1999, and the Ph.D. degree in mechanical engineering from the Harbin Institute of Technology (HIT), Harbin, in 2007, where he is currently an Associate Professor and a Ph.D. Supervisor with the School of Mechatronics Engineering.

His main research interests include bionic robots and mechatronics devices.

GANGFENG LIU (M'11) received the B.S., M.S., and Ph.D. degrees in mechanical engineering from the Harbin Institute of Technology (HIT), Harbin, China, in 2003, 2005, and 2010, respectively, where he is currently an Assistant Professor and a M.S. supervisor with the School of Mechatronics Engineering.

His research interests include autonomous learning, compliant control, and mechanism optimization.

XUEHE ZHANG received the B.S. and M.S. degrees in computer science and technology from the University of Science and Technology Liaoning, Anshan, China, in 2008 and 2011, respectively, and the Ph.D. degree in mechanical engineering from the Harbin Institute of Technology (HIT), Harbin, China, in 2016.

He is currently a Research Assistant with the School of Mechatronics Engineering, HIT. His research interests include robot vision, deep learning, and semantic SLAM.

MINGZHU LAI received the B.S. degree in computer science and technology from the Harbin University of Science and Technology (HUST), Harbin, China, in 2003, and the Ph.D. degree in computer application technology from Harbin Engineering University (HEU), Harbin, in 2017. She is currently an Associate Professor with the School of Mathematics and Statistics, Hainan Normal University.

Her research interests include pattern recognition, image processing, and information hiding.

MO LI received the B.S. degree in mechanical engineering from the Harbin Institute of Technology (HIT), Harbin, China, in 2017, where he is currently pursuing the M.S. degree with the School of Mechatronics Engineering.

His research interests include reconfigurable modular robots, wearable rehabilitation robots, and bionic robots.

TIANJIAO ZHENG received the B.S. and M.S. degrees in mechanical engineering from the Harbin Institute of Technology (HIT), Harbin, China, in 2012 and 2014, respectively, where he is currently pursuing the Ph.D. degree with the School of Mechatronics Engineering.

His research interests include nonlinear dynamics, wearable rehabilitation robots, and bionic robots.

GUOAN ZHANG received the B.S. and M.S. degrees in mechanical engineering from Northeast Electric Power University, Jilin, China, in 2010 and 2013, respectively, and the Ph.D. degree in mechatronics engineering from the Harbin Institute of Technology (HIT), Harbin, China, in 2018.

He is currently a Lecturer with the School of Aeronautical Engineering, Taizhou University. His research interests include robotic vision, wearable rehabilitation robots, and robotic exoskeleton.

JIE ZHAO (M'05) received the B.S. and Ph.D. degrees in mechatronics engineering from the Harbin Institute of Technology (HIT), Harbin, China, in 1990 and 1996, respectively, where he is currently a Professor and a Ph.D. Supervisor with the School of Mechatronics Engineering.

He is also the Leader of the Subject Matter Expert Group, Intelligent Robot in National Key R&D Program, supervised by the Ministry of Science and Technology of China. His research interests include design, modeling, and control of bionic robots and industrial robots.

YANHE ZHU (M'08) received the B.S. and Ph.D. degrees in mechatronics engineering from the Harbin Institute of Technology (HIT), Harbin, China, in 1998 and 2004, respectively, where he is currently a Professor and a Ph.D. Supervisor with the School of Mechatronics Engineering.

He is also the Deputy Director of the State Key Laboratory of Robotics and System. His research interests include reconfigurable modular robots and robotic exoskeletons.